

## Multiscale Structure and Evolution of Hurricane Earl (2010) during Rapid Intensification

ROBERT F. ROGERS AND PAUL D. REASOR

*Hurricane Research Division, NOAA/Atlantic Oceanographic and Meteorological Laboratory, Miami, Florida*

JUN A. ZHANG

*Cooperative Institute for Marine and Atmospheric Studies, University of Miami, Miami, Florida*

(Manuscript received 3 June 2014, in final form 8 September 2014)

### ABSTRACT

The structure and evolution of Hurricane Earl (2010) during its rapid intensification as sampled by aircraft is studied here. Rapid intensification occurs in two stages. During the early stage, covering  $\sim 24$  h, Earl was a tropical storm experiencing moderate northeasterly shear with an asymmetric distribution of convection, and the symmetric structure was shallow, broad, and diffuse. The upper-level circulation center was significantly displaced from the lower-level circulation at the beginning of this stage. Deep, vigorous convection—termed convective bursts—was located on the east side of the storm and appeared to play a role in positioning the upper-level cyclonic circulation center above the low-level center. By the end of this stage the vortex was aligned and extended over a deep layer, and rapid intensification began. During the late stage, rapid intensification continued as Earl intensified  $\sim 20 \text{ m s}^{-1}$  during the next 24 h. The vortex remained aligned in the presence of weaker vertical shear, although azimuthal asymmetries persisted that were characteristic of vortices in shear. Convective bursts concentrated near the radius of maximum winds, with the majority located inside the radius of maximum winds. Each of the two stages described here raises questions about the role of convective- and vortex-scale processes in rapid intensification. During the early stage, the focus is on the role of convective bursts and their associated mesoscale convective system on vortex alignment and the onset of rapid intensification. During the late stage, the focus is on the processes that explain the observed radial distribution of convective bursts that peak inside the radius of maximum winds.

### 1. Introduction

Progress in tropical cyclone (TC) intensity forecasts has lagged that of track forecasts (Rogers et al. 2006, 2013a, hereafter R13; DeMaria et al. 2014), largely because of the multiscale nature of the processes responsible for intensity change (Marks and Shay 1998). Rapid intensification (RI), defined as an increase in the peak 10-m winds of  $\sim 15 \text{ m s}^{-1}$  in 24 h, is particularly challenging, as well as important, to predict. Much research has been devoted to better understanding these processes across the spatiotemporal range of scales, ranging from the environmental scale down to the microphysical scale.

Some skill at predicting RI has been attained by using algorithms that rely primarily on environmental-scale parameters (Kaplan et al. 2010). However, there is much room for improvement, suggesting that processes operating on scales smaller than the environmental scale also contribute to intensity change (Hendricks et al. 2010).

Vortex, convective, and boundary layer processes have been examined as subsynoptic-scale contributors to RI. The symmetric vortex-scale processes involved with TC intensification, involving the cooperative interaction between the symmetric primary and secondary circulation patterns and the impact of axisymmetric diabatic heating on this interaction, have been emphasized in numerous studies (e.g., Ooyama 1969, 1982; Schubert and Hack 1982; Nolan and Grasso 2003; Nolan et al. 2007), while asymmetric processes such as vertical wind shear (e.g., Reasor et al. 2009; Molinari and Vollaro 2010; Reasor and Eastin

---

Corresponding author address: Robert Rogers, Hurricane Research Division, NOAA/AOML, 4301 Rickenbacker Causeway, Miami, FL 33149.

E-mail: robert.rogers@noaa.gov

2012; Nguyen and Molinari 2012) and eye–eyewall mixing (e.g., Schubert et al. 1999; Kossin and Schubert 2001; Kossin and Eastin 2001; Montgomery et al. 2002; Persing and Montgomery 2003; Cram et al. 2007; Nguyen et al. 2011) were identified as important contributors to intensification.

Convection and its role in RI has focused primarily on the role of convective bursts (CBs; i.e., locations of deep, vigorous convection characterized by cold and expanding cloud tops, ice scattering, frequent lightning, and towers of high reflectivity) (Cecil et al. 2002). Bursts have been identified as being associated both with tropical cyclogenesis and RI (Guimond et al. 2010; Rogers 2010; Houze et al. 2009; Reasor et al. 2009; Squires and Businger 2008; Hennon 2006; Kelley et al. 2004; Rodgers et al. 1998; Gentry et al. 1970). The exact role that CBs play has been tied to warming from upper-level subsidence around the periphery of the bursts (Chen and Zhang 2013; Zhang and Chen 2012; Guimond et al. 2010; Heysmsfield et al. 2001) and to the stretching and subsequent axisymmetrization of low-level vorticity collocated with the updraft in vortical hot towers (VHTs; Houze et al. 2009; Reasor et al. 2009; Montgomery et al. 2006; Hendricks et al. 2004). While CBs have received the most attention in terms of convective impacts on RI, some studies have instead emphasized the importance of weak-to-moderate updrafts. Using satellite-based climatologies, Jiang (2012) and Kieper and Jiang (2012) did not find a statistically significant relationship between CBs and intensification. Rather, they found that the azimuthal coverage of precipitation, indicated by a ring of precipitation in 37-GHz microwave images that highlights rainfall and weak-to-moderate updrafts, was a more robust indicator of RI. The relative importance of deep versus moderate/shallow convection in TC intensification and RI is an area of debate, and research is ongoing to address it.

Boundary layer impacts on RI have been studied by Montgomery et al. (2014), Sanger et al. (2014), Montgomery and Smith (2012), and Smith et al. (2009). In their work they discuss two modes of radial inflow and describe how they each lead to changes in the TC structure and intensity. The first mode consists of a deep, relatively weak inflow that converges absolute angular momentum above the boundary layer, where it is conserved. Montgomery et al. (2014) term this the “conventional” mode, based on the earlier work of Ooyama (1969, 1982). The second mode comprises strong inflow in the lowest 1 km that also converges angular momentum, though this quantity is not conserved. This boundary layer inflow spins up the vortex by creating supergradient flow as the inflowing air converges absolute angular momentum at a rate that exceeds its dissipation to the ocean surface via friction. Evidence of this supergradient flow

was shown in dropsonde measurements in Hurricane Earl (2010) (Montgomery et al. 2014) and Supertyphoon Jangmi (2008) (Sanger et al. 2014).

The work discussed above consists of observational or numerical modeling case studies. Another approach to follow is to perform composites to compare the inner-core structure of TCs that intensify with those that do not. The benefit of a composite approach is that statistical robustness can be evaluated. Using composites of airborne Doppler measurements, R13 compared the vortex- and convective-scale structure of hurricanes that intensify with those that remain steady state. They found numerous statistically significant differences between intensifying and steady-state hurricanes, many of which have been identified by previous observational and modeling work. For intensifying storms, key vortex-scale features include a ringlike axisymmetric vorticity structure inside the radius of maximum wind (RMW); lower vorticity in the outer core; a deeper, stronger inflow layer; stronger axisymmetric eyewall upward motion; and a greater azimuthal coverage of precipitation compared with steady-state TCs. Many of these results are similar to those found in previous studies (e.g., Kossin and Eastin 2001; Mallen et al. 2005; Jiang 2012; Kieper and Jiang 2012).

On the convective scale, R13 found that the primary difference between intensifying and steady-state hurricanes was in the distribution of eyewall vertical velocity at the high end of the vertical velocity spectrum. Intensifying storms were found to have a larger number of CBs in the eyewall. The most statistically significant difference found in R13 was the radial location of CBs. For intensifying hurricanes the peak in the CB distribution was preferentially located inside the RMW, where the axisymmetric vorticity is generally higher, whereas for steady-state hurricanes the CBs were primarily located outside the RMW. Such a difference in the radial distribution of CBs was deemed important based on the balance arguments invoked by Shapiro and Willoughby (1982), Schubert and Hack (1982), Nolan et al. (2007), Pendergrass and Willoughby (2009), and Vigh and Schubert (2009). These studies emphasized that the response of a vortex to diabatic heating is dependent on many characteristics of the vortex and heating, such as the radial location of the heating relative to the RMW, the strength of the storm itself, and the horizontal and vertical extent of the circulation. These characteristics determine the efficiency with which diabatic heating released within the storm core is converted into an increase in the kinetic energy of the storm.

While the composite results of R13 show relationships between vortex- and convective-scale properties and TC intensity change in a statistically robust manner, there were some limitations in their study. For one thing, because of sampling limitations only TCs of hurricane

strength were included in the composite. However, RI often begins before a TC reaches hurricane strength (Hennon 2006; Kaplan et al. 2010), so information on the structures associated with the onset of RI is lacking. Also, composites lack the temporal continuity to provide information on the mechanisms underlying the relationships mentioned above. In particular, the role that deep convection, and CBs in particular, play in RI is one that could not be addressed, despite its importance in distinguishing intensifying from steady-state hurricanes.

Hurricane Earl (2010) was a system that underwent RI in the western Atlantic in August 2010. It was intensively sampled by a multitude of aircraft during most of its lifetime (Rogers et al. 2013b; Braun et al. 2013; Montgomery et al. 2014; Uhlhorn et al. 2014), including the National Oceanic and Atmospheric Administration (NOAA) WP-3D and G-IV, the National Aeronautics and Space Administration (NASA) DC-8 and Global Hawk, and the Air Force C-130 aircraft. The NOAA WP-3D aircraft sampled Earl at 12-h intervals beginning before RI, when it was a  $25 \text{ m s}^{-1}$  tropical storm, during RI, and at the end of RI  $\sim 60 \text{ h}$  later, when it was a  $\sim 55 \text{ m s}^{-1}$  category 3 hurricane. The temporal coverage provided by these flights provides an opportunity to study the impact of CBs on the onset and subsequent extended period of RI. Additionally, dropsondes released by all aircraft during one period of RI (discussed later) provide excellent coverage of the boundary layer kinematic structure that provides insight into the mechanisms underlying the observed radial distribution of CBs for Earl.

The study shown here is organized as follows. Section 2 provides a description of the dataset used in the Earl analysis. Section 3 provides an overview of Earl's RI, including a description of the environmental conditions and symmetric vortex structure and evolution. Section 4 discusses two stages of Earl's RI: the early stage, including RI onset, when Earl transitions from a disorganized to a vertically coherent tropical storm in moderate shear; and the late stage, when Earl accomplishes the bulk of its intensification in light shear as CBs are primarily concentrated just inside the RMW. Section 5 presents a discussion of the role of the CBs during each of these stages, with the focus on how the CBs, and their associated mesoscale convective system, may impact the alignment of Earl during the early stage; and what mechanisms during the late stage are responsible for the observed distribution of CBs inside the RMW for Earl, as identified by comparison with a different radial distribution for a steady-state case.

## 2. Dataset

The data used in this study come from aircraft missions flown into Hurricane Earl during the period during

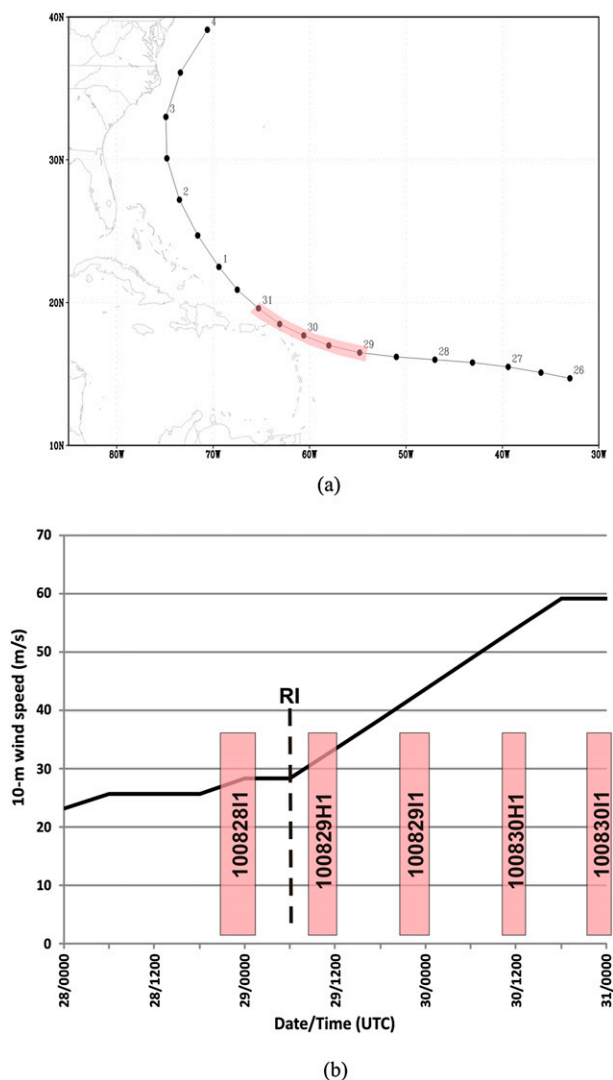


FIG. 1. (a) Best track position of Hurricane Earl; time period covered by WP-3D flights considered here indicated by the pink shaded box. (b) Best track intensity ( $\text{m s}^{-1}$ ). Approximate on-station times of WP-3D missions indicated by pink boxes. Onset of RI indicated by the bold dashed line. Flight identification numbers for each mission are indicated in boxes.

28–31 August 2010. A multitude of aircraft flew missions in this storm during nearly its entire life cycle, including prior to the onset of RI, through RI, and later in its life cycle when it was a mature hurricane undergoing eyewall replacement cycles. These aircraft included the NOAA WP-3D and G-IV aircraft as part of the NOAA Intensity Forecasting Experiment (IFEX; R13), the NASA DC-8 and Global Hawk aircraft as part of the NASA Genesis and Rapid Intensification Processes Experiment (GRIP; Braun et al. 2013), and the Air Force C-130 aircraft. The time of focus for this study is during the pre-RI and RI periods, which include five WP-3D (cf. Fig. 1b, Table 1),

TABLE 1. Key parameters during the WP-3D missions in Earl.

Mission ID	Approximate center time	Intensity ( $\text{m s}^{-1}$ )	RMW (km)	Storm $u$ ( $\text{m s}^{-1}$ )	Storm $v$ ( $\text{m s}^{-1}$ )	850–200-hPa shear magnitude ( $\text{m s}^{-1}$ )	850–200-hPa shear heading ( $^{\circ}$ )
100828I1	0000 UTC 29 Aug	28.3	65	−9.6	1.7	9.3	223
100829H1	1200 UTC 29 Aug	33.4	101	−8.4	1.5	7.7	220
100829I1	0000 UTC 30 Aug	43.7	49	−7.2	1.9	4.6	205
100830H1	1200 UTC 30 Aug	54.0	35	−7.2	1.9	3.1	122
100830I1	0000 UTC 31 Aug	59.1	23	−5.9	3.4	5.9	153

three G-IV, two DC-8, and four C-130 missions. Based on the best track analysis shown in Fig. 1b, Earl's RI began during the second flight.

The analysis presented here relies primarily on data obtained from the X-band tail Doppler radar on board the NOAA WP-3D aircraft. Analyses from this data are derived from a variational algorithm (Gamache 1997) that takes the measured reflectivity and Doppler radial velocity to produce gridded three-dimensional analyses. This algorithm simultaneously solves the continuity and Doppler projection equations using least squares minimization (Reasor et al. 2009) to produce grids with horizontal and vertical spacings of 2 and 0.5 km, respectively. Studies using this variational analysis technique include the RI studies of Guillermo (e.g., Reasor et al. 2009; Reasor and Eastin 2012). An automated version of this algorithm has been developed that substantially reduces the length of time needed to perform the quality control and synthesis of the radar data while still preserving error characteristics comparable to those obtained through manual quality control (Rogers et al. 2012). Analyses using this automated version have been used in the composite and case studies of Stern and Nolan (2009, 2011), Rogers et al. (2012, R13), Reasor et al. (2013), Hazelton and Hart (2013), and DeHart et al. (2014).

In addition to the Doppler analyses, GPS dropsondes (Hock and Franklin 1999) are used to document the lower-level and boundary layer thermodynamic and kinematic structure of Earl. With a fall speed of 12–14  $\text{m s}^{-1}$  and a typical sampling rate of 2 Hz, measurements with 6–7 m spacing in the vertical are available. Dropsondes have been used in numerous studies over the past 15 years, including recent composite-based studies of the axisymmetric and asymmetric structure of the boundary layer of mature tropical cyclones (Zhang et al. 2011, 2013) and the boundary layer structure during the rapid intensification of Hurricane Earl (Montgomery et al. 2014) and Super-typhoon Jangmi (Sanger et al. 2014). Dropsondes from all aircraft used in this analysis were postprocessed using the National Center for Atmospheric Research's (NCAR's) Atmospheric Sounding Processing Environment (ASPEN) software. Recent studies have shown little difference between ASPEN-processed data compared to those

processed by the Editsonde software developed by the Hurricane Research Division (Franklin et al. 2003).

The WP-3D missions flown in Earl consisted of a series of radial passes with an azimuthal separation of 45°–60°. Given Earl's proximity to the base of operations for the WP-3D (Barbados during this series of flights), the time within the storm was maximized. As a result "rotating figure-4" patterns (azimuthal separation of 45° between radial passes) were flown for the first three flights, while "butterfly" patterns (azimuthal separation of 60° between passes) were flown for the fourth and fifth flights. Individual radial passes, which generally take ~1 h to complete, can be merged into a single analysis that represents the conditions of the vortex over the time scale of the flight pattern (typically ~4–5 h; Rogers et al. 2012). For the depiction of more slowly evolving vortex-scale parameters that require greater spatial coverage (e.g., axisymmetric fields and horizontal flow), merged analyses are used. For smaller-scale and more rapidly evolving convective-scale fields, individual passes are used. A similar analysis approach was followed in Rogers et al. (2012) and R13.

### 3. Overview of Earl's RI

Earl developed from a strong tropical wave that emerged off the coast of Africa in late August 2010. The system was declared a tropical depression by the National Hurricane Center at 0600 UTC 25 August when it was west-southwest of the Cape Verde Islands (Fig. 1a), and within 6 h the system had become well organized enough to be declared a tropical storm. Earl moved toward the west and west-northwest at ~7  $\text{m s}^{-1}$ , slowly intensifying during this time. By 1200 UTC 28 August, just prior to the first NOAA aircraft missions (Fig. 1b), Earl had intensified to a moderate tropical storm of ~25  $\text{m s}^{-1}$  (Table 1). Over the next 24 h Earl slowed its forward motion and turned more toward the northwest, just to the northeast of the Leeward Islands. Just prior to the second WP-3D mission, around 0600 UTC 29 August, the intensification rate, based on the best track analysis, increased significantly. This is identified as the onset of RI. The best track intensity increased ~30  $\text{m s}^{-1}$  during the next three missions, reaching ~60  $\text{m s}^{-1}$  by

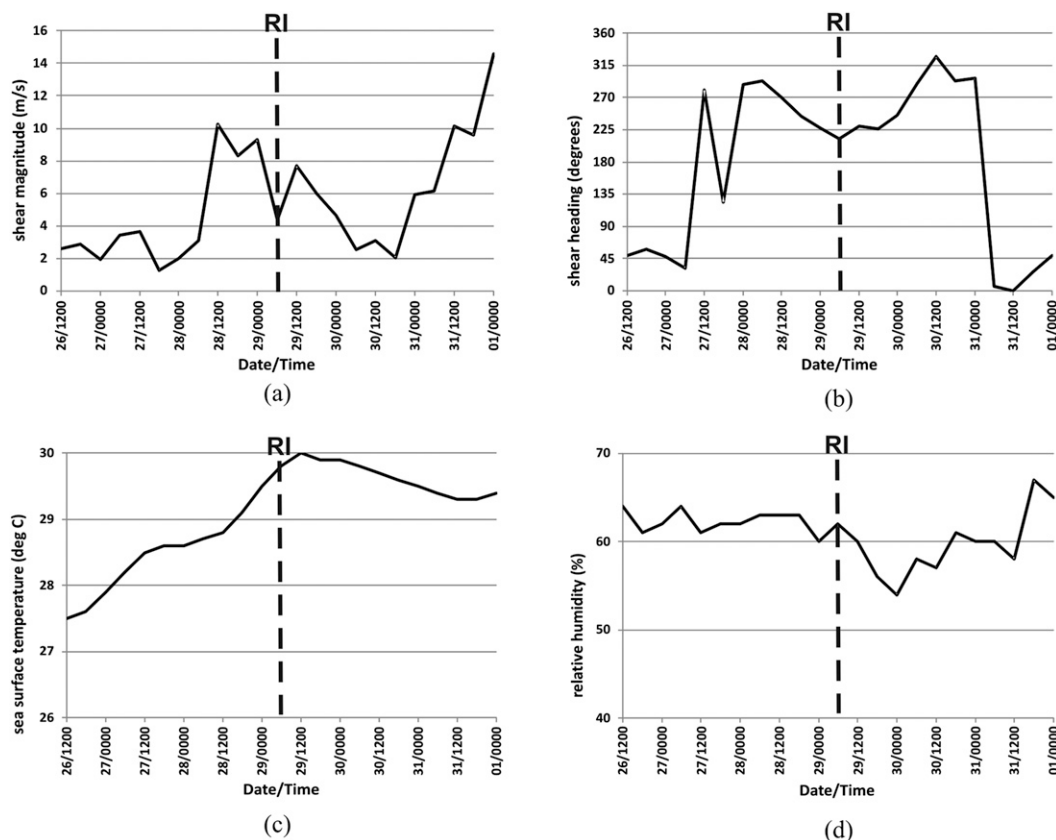


FIG. 2. Time series of large-scale environmental parameters from GFS analyses at times indicated along abscissa, where 26/1200 = 1200 UTC 26 Aug, etc. (a) 850–200-hPa vertical shear magnitude ( $\text{m s}^{-1}$ ); (b) 850–200-hPa vertical shear heading ( $^{\circ}$ ,  $0^{\circ}$  = shear toward east,  $90^{\circ}$  = shear toward north, etc.) averaged within 0–500 km of the center; (c) sea surface temperature at storm center ( $^{\circ}\text{C}$ ); and (d) relative humidity averaged in 850–700-hPa layer (%) in 200–800-km radius. The dashed line indicates the time of RI onset based on best track data.

0000 UTC 31 August. At this point an eyewall replacement cycle began, halting further intensification for the following 24 h (Cangialosi 2010; Braun et al. 2013). The time period described here (i.e., prior to and during RI) is the focus of this study.

The environment of Earl prior to the first aircraft missions is generally favorable for development. Figure 2 shows environmental parameters derived from the Statistical Hurricane Intensity Prediction Scheme (SHIPS; DeMaria et al. 2005). These SHIPS analyses are obtained from operational global model analyses produced by the Global Forecast System (GFS) model. Vertical shear in this analysis is computed from a 0–500-km radius after the vortex had been removed (Kaplan et al. 2010). From 1200 UTC 26 August to 0600 UTC 28 August, the 850–200-hPa vertical shear is low (Fig. 2a), with values  $<4 \text{ m s}^{-1}$ . By 1200 UTC 28 August the shear increases, reaching a value of  $\sim 9 \text{ m s}^{-1}$  by 0000 UTC 29 August from the northeast, as Earl interacts with the outflow of Hurricane Danielle (Fig. 3) to the north. The shear as analyzed by SHIPS does temporarily drop below  $5 \text{ m s}^{-1}$

at the onset of RI at 0600 UTC 29 August, but then returns to near  $8 \text{ m s}^{-1}$  six hours later. Additionally, as Earl progresses toward the west and west-northwest the SST steadily increases to nearly  $30^{\circ}\text{C}$  (Figs. 2c and 3). It is during this time of moderate shear and increasing SST that RI begins. Shortly after RI begins the shear decreases to near  $4 \text{ m s}^{-1}$  (Fig. 2a, Table 1) as Danielle pulls away to the north (Fig. 3). The RI continues during this time, with Earl reaching major hurricane status. After the end of the fifth WP-3D flight, the shear increases again as Earl begins to recurve while interacting with an upper-level trough.

The relative humidity from the GFS analyses averaged in the 850–700-hPa layer (Fig. 2d) and between the 200- and 800-km radius show values around 60% in the environment of Earl during the 48 h leading up to RI. Humidity values from this analysis decrease slightly to 55% once RI begins before increasing to 65% toward the end of the period. A more detailed analysis of the thermodynamic environment around Earl (Braun et al. 2013) showed that Earl underwent RI even though a Saharan

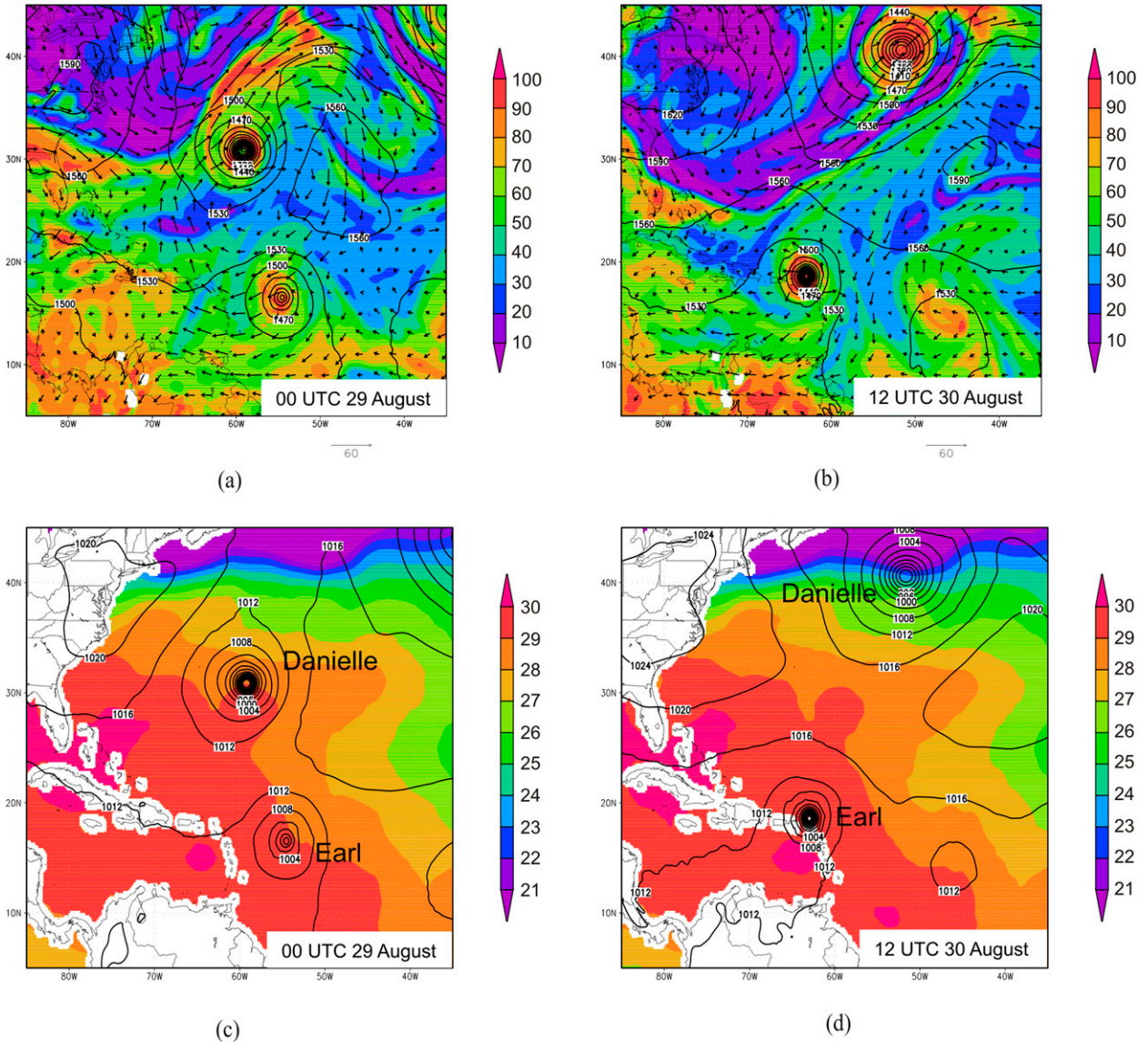


FIG. 3. (a) GFS analysis of 700-hPa relative humidity (shaded, %), 850-hPa geopotential height (contour, m), and 200-hPa flow (vector,  $\text{m s}^{-1}$ ) valid at 0000 UTC 29 Aug. (b) As in (a), but for 1200 UTC 30 Aug. (c) GFS analysis of sea surface temperature (shaded,  $^{\circ}\text{C}$ ) and sea level pressure (contour, hPa) valid at 0000 UTC 29 Aug. (d) As in (c), but for 1200 UTC 30 Aug. Locations of Hurricane Danielle and Tropical Storm/Hurricane Earl are indicated in (c) and (d).

air layer (SAL) was in the vicinity. Using dropsondes from the G-IV and DC-8 aircraft, [Braun et al. \(2013\)](#) showed high 700-hPa relative humidity values within the inner 200 km, while values at larger radii dropped significantly (to  $\sim 30\%$ ) on the north and west side ([Fig. 3](#)), coincident with high dust concentrations associated with the SAL. This pattern persisted for the entire RI period. [Braun et al. \(2013\)](#) attributed this ability of Earl to undergo RI in the presence of a dry environment to the fact that it was embedded in a protective wave “pouch,” similar to that discussed in [Dunkerton et al. \(2009\)](#) and [Montgomery et al. \(2012\)](#).

[Figure 4](#) shows the storm-relative wind speed at 2-km altitude obtained from the merged analyses from each of the five WP-3D missions. During the first mission the peak 2-km winds are  $30 \text{ m s}^{-1}$  in isolated areas in a band located about 60 km on the east side of the center. By the second mission this area of  $30 \text{ m s}^{-1}$  winds expands, but the band in which it is located shifts to a radius  $\sim 100$  km from the center. Additionally, a small area of locally stronger wind is located much closer to the center. During the third mission, after RI had been occurring for  $>12$  h, a ring of wind speed  $>30 \text{ m s}^{-1}$  surrounds the storm, and areas  $>35 \text{ m s}^{-1}$  are also evident. Earl had

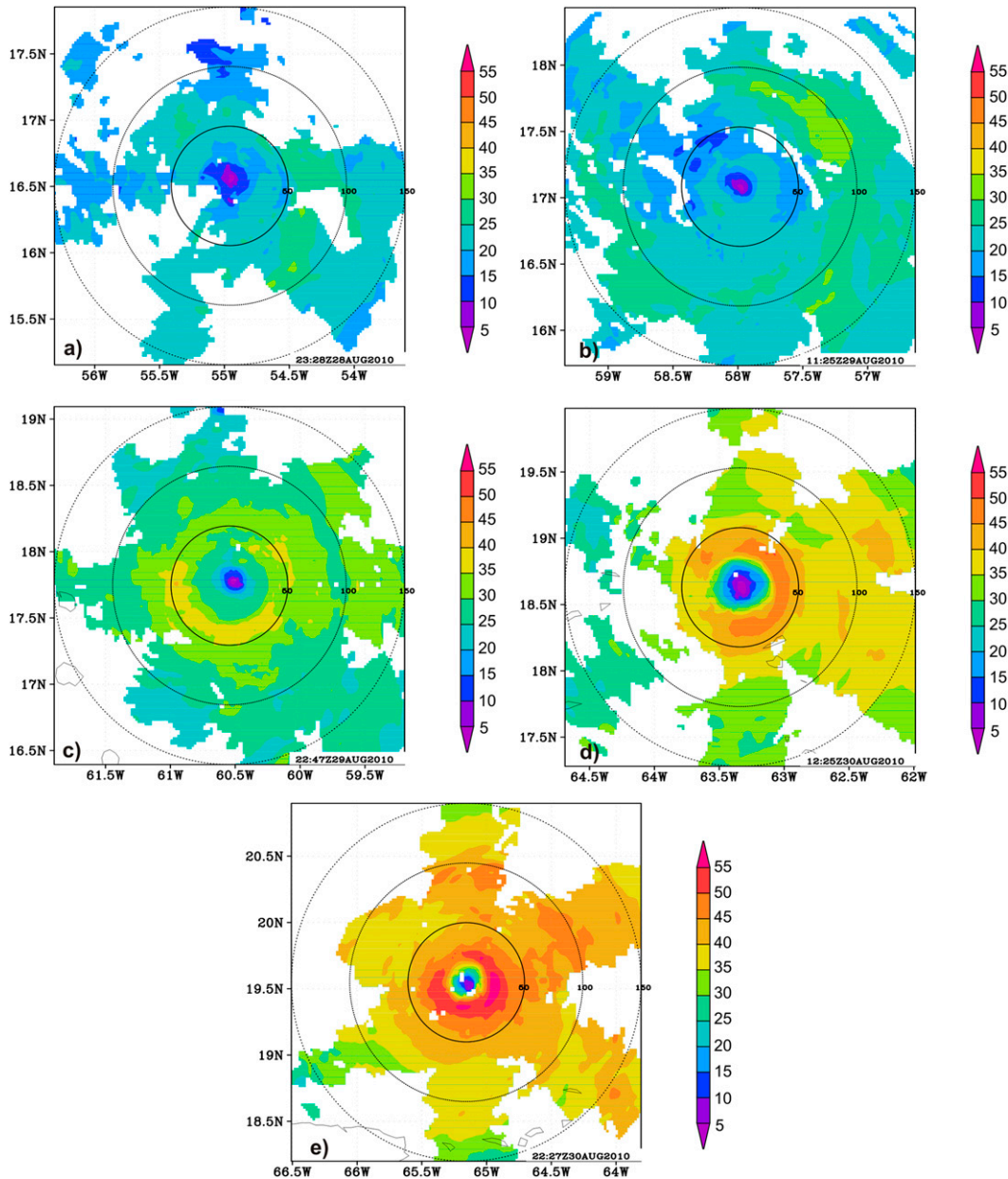


FIG. 4. Doppler-derived storm-relative wind speeds (shaded,  $\text{m s}^{-1}$ ) at 2-km altitude for missions (a) 100828I1, (b) 100829H1, (c) 100829I1, (d) 100830H1, and (e) 100830I1. Times indicated in right-hand corner are center times for the merged radar analyses. Dashed circles are range rings plotted every 50 km.

begun to contract as well, as the RMW is  $\sim 50$  km. By the fourth flight, winds exceed  $45 \text{ m s}^{-1}$  in a band about 35 km from the center, and during the fifth flight the winds now are  $>55 \text{ m s}^{-1}$  at a radius of  $\sim 25$  km.

Radius–height cross sections of axisymmetric tangential wind and vorticity (Fig. 5) show that Earl's circulation is shallow during the first two missions. During the first mission the tangential wind maximum only extends up to  $\sim 6$  km. A similar structure was seen during the second mission, though the circulation showed a local maximum

at  $\sim 25$  km seen in Fig. 5 and a broad maximum located near 100 km. A clear change in the vertical structure of Earl is seen by the third mission, as the tangential wind maximum extends to a higher altitude and the storm has contracted. By the fourth and fifth missions, Earl is a well-developed hurricane with a deep, strong primary circulation. Outside the RMW the tangential winds increase during the third to fifth missions, a pattern that commonly occurs as rainbands develop and concentrate localized regions of vorticity outside the inner core, sometimes

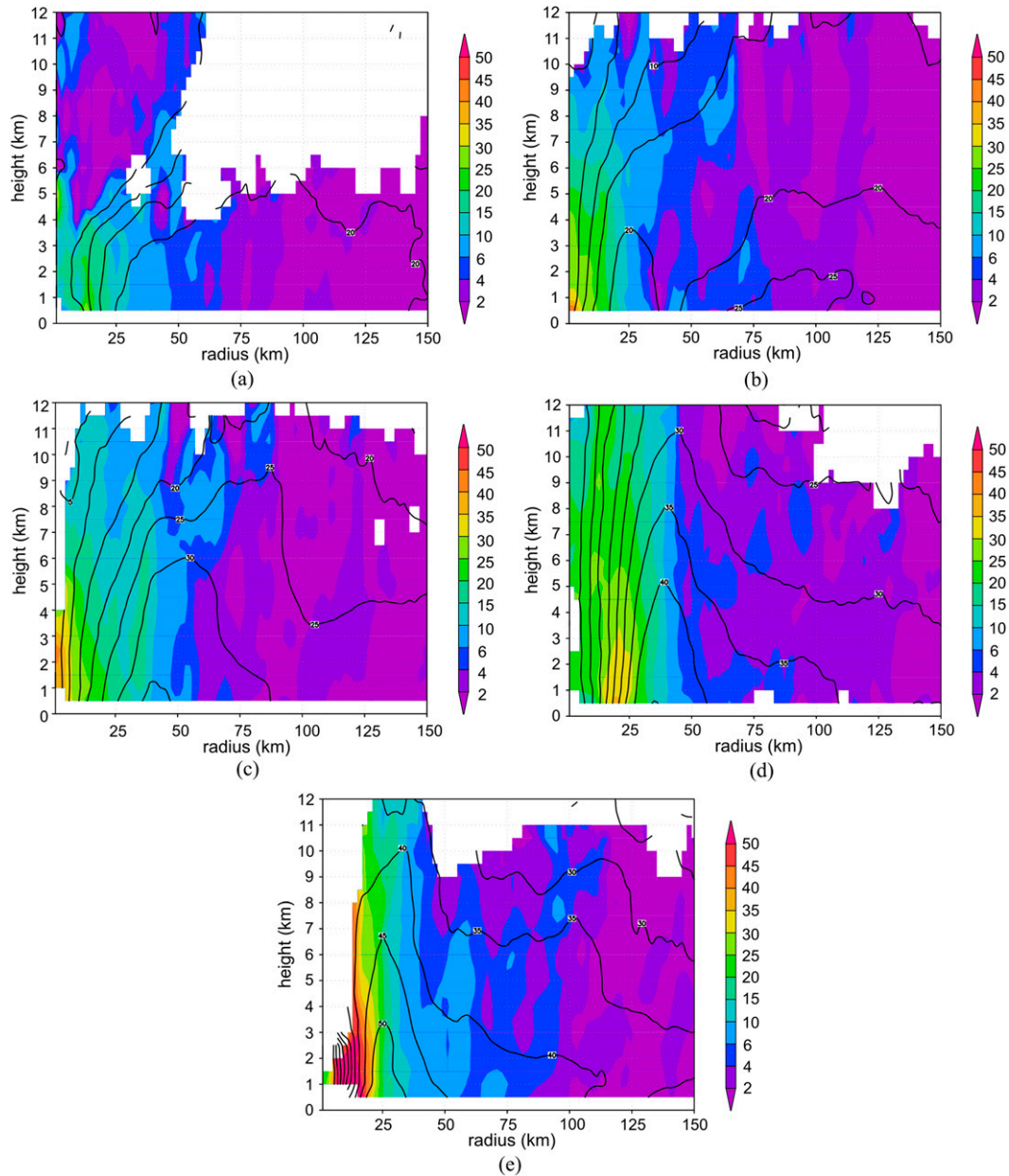


FIG. 5. Radius–height cross sections of axisymmetric vorticity (shaded,  $\times 10^{-4} \text{ s}^{-1}$ ) and axisymmetric tangential wind (contour,  $\text{m s}^{-1}$ ) for missions (a) 100828I1, (b) 100829H1, (c) 100829I1, (d) 100830H1, and (e) 100830I1. Locations with more than  $180^\circ$  of a contiguous gap are not plotted.

leading to secondary eyewall formation (e.g., [Didlake and Houze 2011](#)).

Similar to the tangential wind, the axisymmetric vorticity field is also shallow during the first mission (cf. [Fig. 5](#)). For the second mission, elevated vorticity extends over a deeper layer, as a region of enhanced radial gradient of tangential wind associated with the inner local maximum extends to 10-km altitude. There is also a weak, shallow signature of vorticity along the inner edge of the outer peak tangential of winds at  $\sim 75$ -km

radius. By the third mission a core of high vorticity is seen within the inner 20 km. Additionally, there is a suggestion of a narrow band of higher vorticity along the inner edge of the tangential wind maximum, extending up to 9-km altitude. Such a ringlike structure in the vorticity field has been seen in previous observational studies of intensifying TC’s ([Kossin and Eastin 2001, R13](#)), and they indicate a regime favorable for the horizontal mixing of vorticity between the eye and eyewall. The fourth mission indicates that this ringlike

vorticity structure is even more pronounced. Additionally, vorticity outside the RMW has increased, particularly outside  $\sim 2 \times$  RMW. By the fifth mission the core vorticity has increased substantially as the RMW has contracted to  $\sim 25$  km. The vorticity outside the RMW has also continued to increase, consistent with an expanding tangential wind field and the eventual development of a secondary eyewall after this time.

The evolution of the symmetric structure described above indicates that there are two stages of Earl's RI. During the early stage, which lasts for the first two missions, the storm encounters moderate vertical shear and its symmetric circulation is shallow, broad, and diffuse. The RI begins just prior to the second mission. During the subsequent three missions the shear drops and the vortex develops a deep primary symmetric circulation whose RMW contracts while intensifying to a major hurricane. The next section will discuss the inner-core structure and evolution of the vortex during these two stages, and the role that deep convection plays during each of the stages.

#### 4. Two stages of Earl's RI

##### *a. Early stage: Alignment of circulation centers in moderate shear*

During the first two missions Earl is characterized by a broad, shallow axisymmetric tangential wind and vorticity field (cf. Figs. 4–5). Figure 6 shows the relative vorticity and storm-relative circulation at 2, 5, and 8 km along with the large-scale (SHIPS derived) 850–200-hPa shear and storm motion vectors at the nearest 6-h time to the mission times. These fields show significant evolution of the vertical structure of Earl between the first and second mission. During the first mission, the circulation center at 2 km is positioned underneath a circulation at 5 km that is elongated in a northwest–southeast orientation. At 8 km, a clear circulation center is displaced  $\sim 50$  km to the east-southeast of the 2-km center. The vorticity field at this time suggests distinct positive vortex cores at lower and upper levels rather than a continuously tilted vortex core with height. Nevertheless, the evolution of these nearby vortex cores may still be understood using the ideas of vortex precession and alignment applied to vertically coherent vortices (Reasor and Montgomery 2001). The direction of displacement of the 8-km center is to the left of the northeasterly large-scale shear vector, consistent with what has been shown in theoretical, numerical, and observational studies of vortices in shear (e.g., Jones 1995; Wang and Holland 1996; Rogers et al. 2003; Reasor et al. 2004; Reasor and Eastin 2012; Reasor et al. 2013), though those studies primarily considered

vortices of hurricane strength. By the time of the second mission 12 h later, the circulations were nearly aligned, despite the presence of moderate shear ( $\sim 6 \text{ m s}^{-1}$ ) persisting from the northeast.

The evolution of the vortex during the first mission can be seen by examining the individual radial passes that compose the merged analyses from Fig. 6. Figure 7 shows the storm-relative flow at 8 km, radar reflectivity at 2 km, and locations of CBs for radial passes during the first mission (centered at 2129 and 2254 UTC 28 August and 0125 UTC 29 August), along with near-coincident sweeps from the lower fuselage (LF) radar. The CBs here are defined as those locations where the maximum vertical velocity<sup>1</sup> in the 8–16-km layer is  $>5 \text{ m s}^{-1}$  and the reflectivity averaged in the 8–14-km layer is  $>20$  dBZ. These criteria were chosen to capture those convective features with strong updrafts in the middle to upper troposphere that transport high reflectivity aloft, similar to the hot tower structures seen in previous spaceborne and airborne studies (e.g., Heymsfield et al. 2001; Cecil et al. 2002; Kelley et al. 2004; Guimond et al. 2010). These deep convective cores, representing the top end of the vertical velocity distribution above the freezing level sampled by airborne Doppler radar near the RMW, were found to be a key convective-scale feature distinguishing intensifying from steady-state hurricanes as shown in R13. They are the focus of the study here.

An asymmetric distribution of high reflectivity and CB activity is apparent during the three passes, with the heaviest precipitation and most vigorous upper-level updrafts confined to the east side of the storm (i.e., left of the deep-layer shear vector, cf. Fig. 6). The LF imagery shows that the primary CB activity near the RMW is located at the downwind end of a band that spirals out toward the south and southwest of the center, with some isolated grid points flagged as CBs at these larger radii. The CB activity near the RMW is seen from both the tail Doppler and LF radars to translate from the southeast to the northeast side of the storm during the  $\sim 4$ -h period covered by these radial passes, passing through an arc left of the shear vector in a manner consistent with that shown in Black et al. (2002). The flow vectors at 8 km show a clear cyclonic curvature associated with the CB. While

---

<sup>1</sup> With a horizontal and vertical grid spacing of 2 and 0.5 km, respectively, the radar analyses will smooth the smallest-scale features, resulting in peak updrafts weaker than those found in studies using higher-resolution analyses (e.g., Heymsfield et al. 2010; Black et al. 1996). However, while the analyses may not precisely represent the exact peaks, they are still able to capture the characteristics (e.g., location, general structure, etc.) of these strong features and are appropriate to use here.

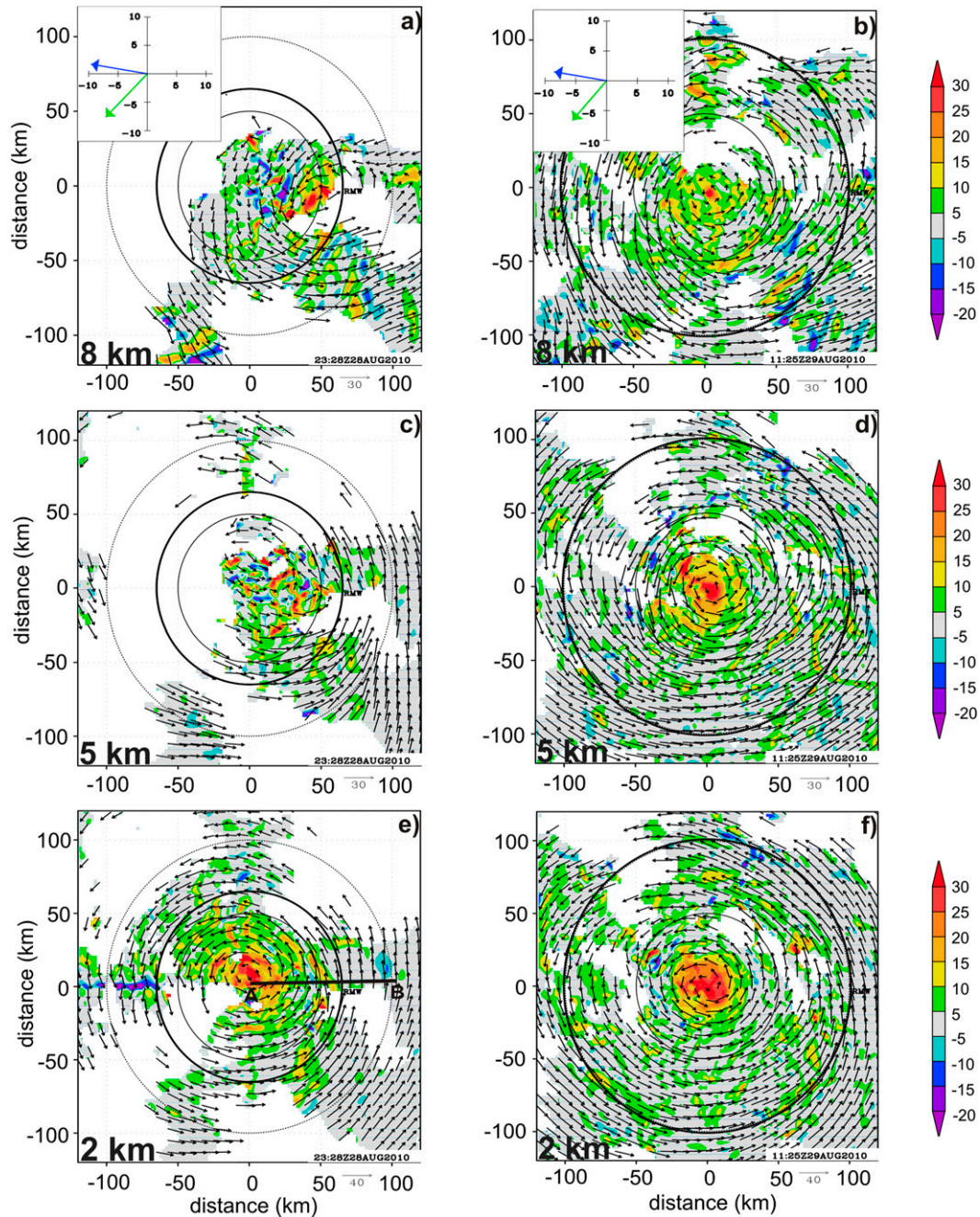


FIG. 6. (a) Vertical vorticity (shaded,  $\times 10^{-4} \text{ s}^{-1}$ ) and flow vectors ( $\text{m s}^{-1}$ ) at 8-km altitude from merged analysis for mission 100828I1. (b) As in (a), but for mission 100829H1. (c) As in (a), but at 5-km altitude. (d) As in (b), but at 5-km altitude. (e) As in (a), but at 2-km altitude. (f) As in (b), but at 2-km altitude. Insets in (a) and (b) show the SHIPS-derived shear vector (green arrow,  $\text{m s}^{-1}$ ) and storm motion vector (blue arrow,  $\text{m s}^{-1}$ ) for the 6-h time nearest to the mission. Line AB in (e) denotes the location of the cross section shown in Fig. 10.

the limited coverage of the wind field near the edges of the analyses precludes a definitive determination of the center location of the cyclonic curvature for each individual pass, it does appear that the center of the cyclonic feature approximately translates with the motion of the burst.

This suggests that the region of cyclonic curvature at 8 km and vigorous convection are linked.

The convective and vortex-scale structure during this time was complex both azimuthally and radially. Figure 8 shows a contoured frequency by altitude diagram (CFAD;

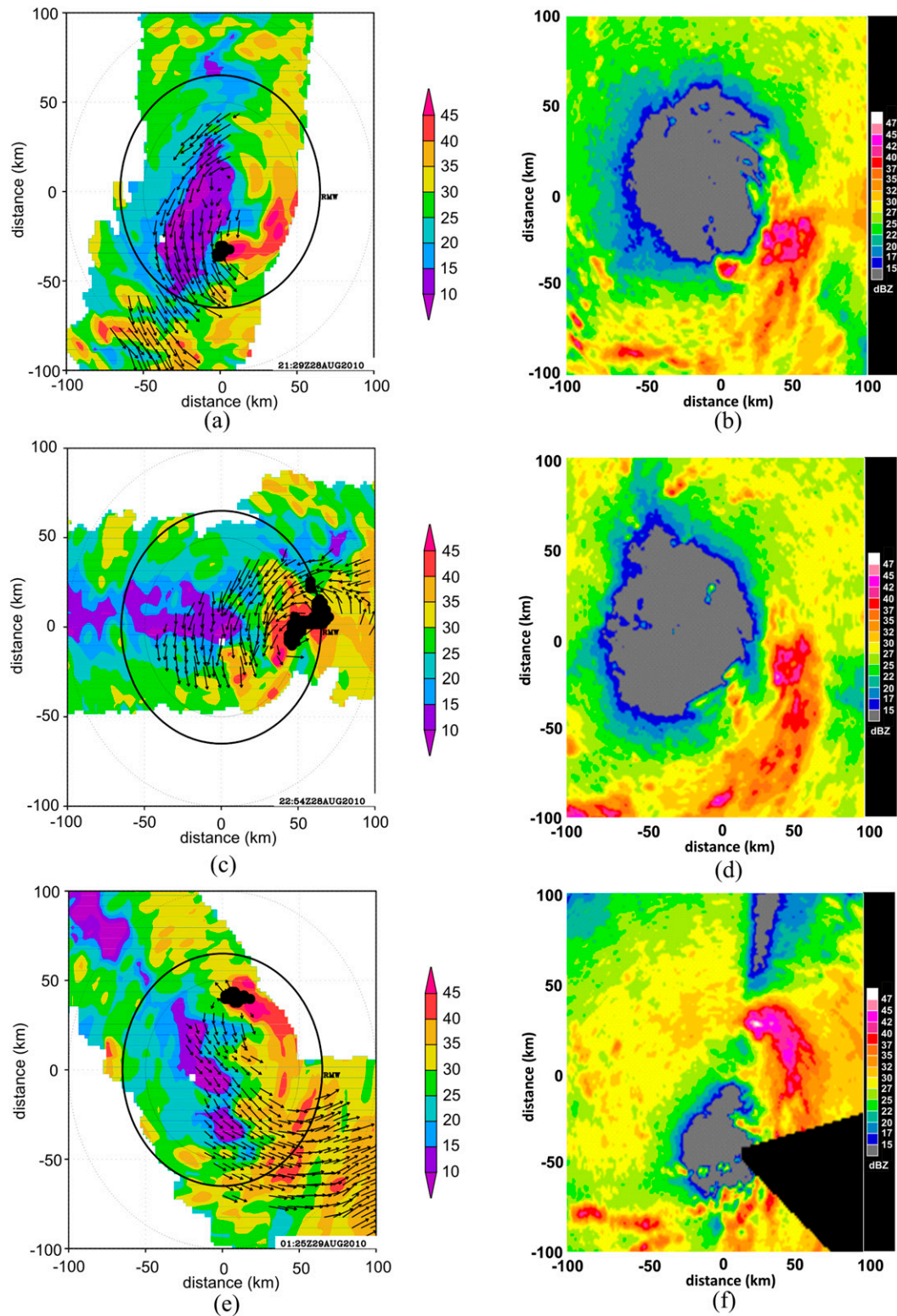


FIG. 7. (a) Reflectivity (shaded, dBZ) at 2-km altitude from tail Doppler radar during an individual radial pass through Earl centered at 2129 UTC 28 Aug. Vectors ( $\text{m s}^{-1}$ ) show storm-relative flow at 8 km. Black dots denote locations of points flagged as convective bursts. RMW at 2-km altitude is indicated by circle. (b) Storm-centered lower-fuselage reflectivity at 3.5 km from a single sweep at 2133 UTC. (c) As in (a), but for a pass centered at 2254 UTC 28 Aug. (d) As in (b), but for a sweep at 2247 UTC. (e) As in (a), but for a pass centered at 0125 UTC 29 Aug. (f) As in (b), but for a sweep at 0125 UTC and at  $\sim 2.5$ -km altitude. Domains in all images are 200 km on a side.

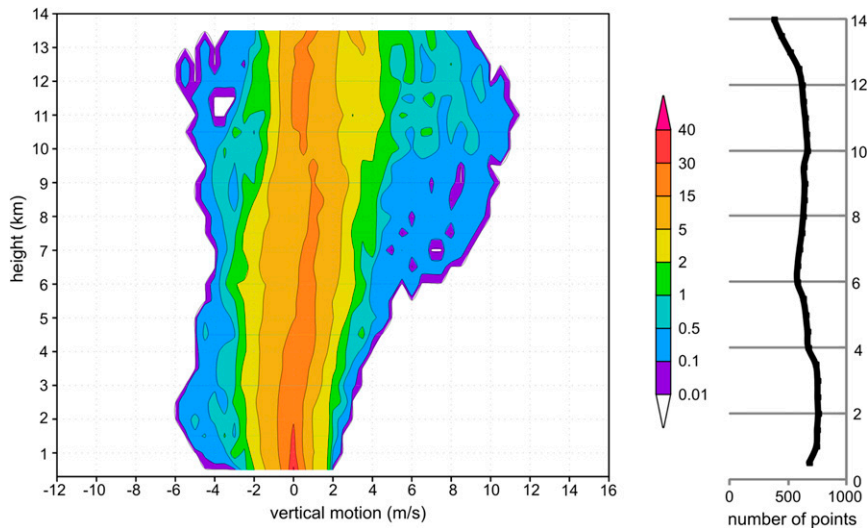


FIG. 8. (left) CFAD of vertical velocity (shaded, %) in the upshear-left quadrant in the radial band between  $0.75 \times \text{RMW}$  and  $1.25 \times \text{RMW}$  from all individual passes from mission 100828H1 shown in Fig. 7. (right) The number of points used to construct the CFAD.

Yuter and Houze 1995) of vertical velocity across the RMW in the upshear-left quadrant, where the CB activity was located for most of the first mission. Peak updrafts  $>10 \text{ m s}^{-1}$  are evident between 8 and 12 km. Below the freezing level (typically  $\sim 5$  km in the tropics) the strongest updrafts are relatively weak, suggesting that the updraft cores aloft occur within parcels advected into the upshear-left quadrant from other regions of the storm. One way this could occur is for updrafts to be advected as they ascend from their location of origin downshear, following the conceptual model shown in Black et al. (2002) and supported by the composite study of DeHart et al. (2014). This evolution is supported by Fig. 9, which shows the azimuthal variation of inflow angle in the boundary layer (i.e., 0.5–2-km layer) and reflectivity across the RMW. The largest inflow angles are located on the west side of the storm (i.e., in the downshear-right quadrant and just to the right of the direction of storm motion). The azimuthal location of the peak inflow is consistent with the shear-relative distribution of radial flow shown in Reasor et al. (2013) and the motion-relative peak surface inflow from dropsonde composites (Zhang and Uhlhorn 2012). The azimuth–height variation of reflectivity (Fig. 9b) shows how the asymmetric structure of reflectivity around the storm discussed previously, particularly above 3 km, is linked with the azimuthal variation of inflow angle. Beginning in the southwest and south parts of the storm, reflectivity increases below the freezing level. Continuing farther downwind around the storm, the height of the elevated reflectivity increases, reaching a maximum where the CB activity is located on the east side. This azimuthal evolution of reflectivity—from a shallow structure on the

right side of the shear vector, to a region of deepening reflectivity cores in the downshear-left quadrant downstream of the peak boundary layer inflow, and ultimately a convective burst in the upshear-left quadrant—is consistent with the notion that updrafts have their roots in the downshear region, similar to what was speculated in the discussion of the CFAD in Fig. 8. Returning to Fig. 8, downdrafts  $<-4 \text{ m s}^{-1}$  extend over the entire depth of the CFAD. Such a distribution of downdrafts in the upshear-left quadrant likely reflects a combination of a balanced vortex response to shear as postulated by Jones (1995) and shown in Reasor et al. (2013) and convectively induced downdrafts as shown in DeHart et al. (2014). Additionally, Black et al. (2002) showed that strong updrafts left of shear were often radially flanked by downdrafts, and Heymsfield et al. (2001) and Guimond et al. (2010) showed strong downdrafts extending from 8 to 14 km adjacent to deep convection.

A cross section extending toward the east from the center during the first mission (Fig. 10), through the upper- and lower-level vorticity centers seen in Fig. 6, shows reflectivity values  $>25$  dBZ that extend above 14 km at 50–75-km radius, associated with the CB activity. Outside this radius is an area of reduced reflectivity above the freezing level and high reflectivity below, indicative of stratiform precipitation. The shallow circulation indicated in Fig. 5 does not extend above the stratiform precipitation at these outer radii. The  $u$  component of the wind (Fig. 10a) shows strong midlevel inflow into the CB, while the  $v$  component (Fig. 10b) shows a region of northerly flow between 5 and 11 km extending  $\sim 60$  km from the center. This flow structure results from the

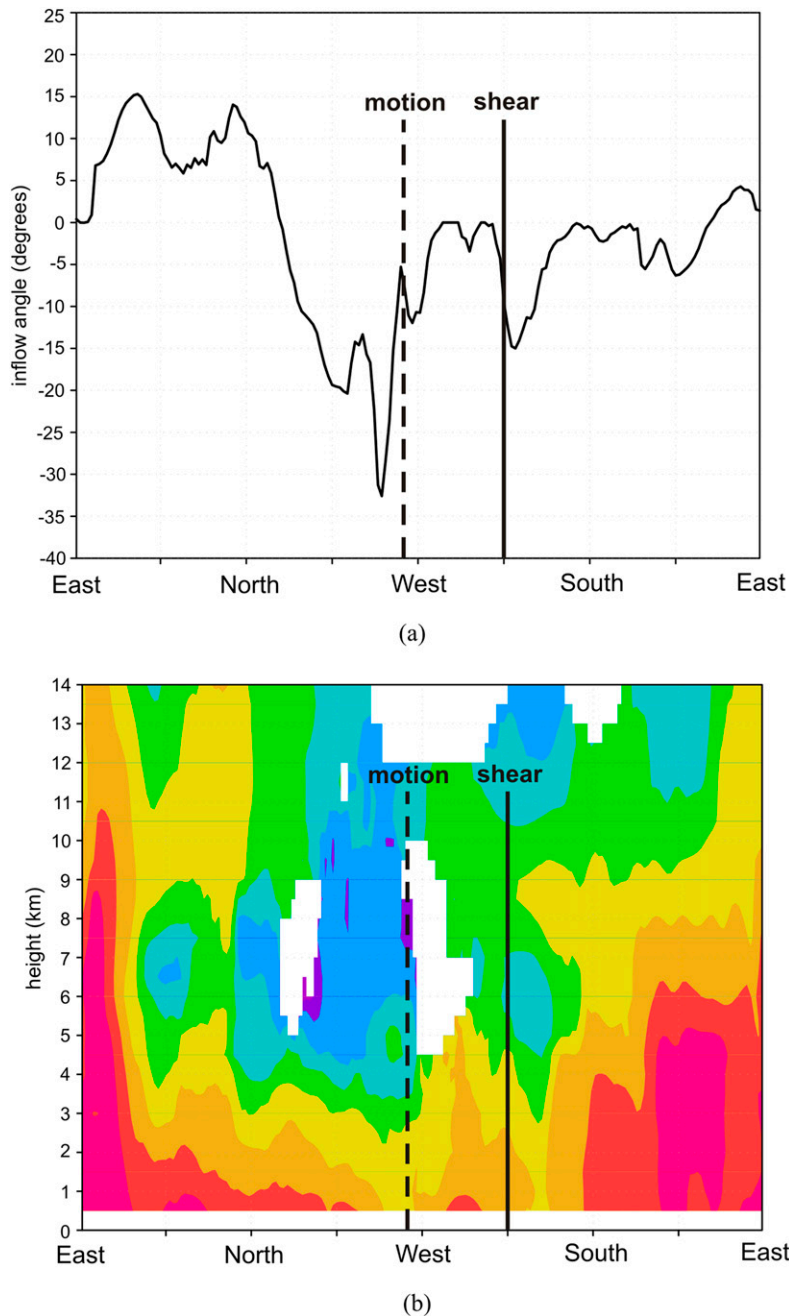


FIG. 9. (a) Azimuthal variation of inflow angle ( $^{\circ}$ , inflow defined as negative) averaged in 0.5–2-km layer in the radial band between  $0.75 \times \text{RMW}$  and  $1.25 \times \text{RMW}$  for mission 100828H1. The solid (dashed) line denotes the direction of 850–200-hPa shear (storm motion) vector. (b) Azimuth–height variation of reflectivity (shaded, dBZ) averaged in the same radial band as in (a).

displacement of the upper-level circulation center toward the east-southeast of the low-level center, as shown in Fig. 6. The vertical velocity shows the strong updraft cores associated with the CB (Fig. 10c). Radially inward from the inner CB is a region of downdrafts with peak values  $< -2.5 \text{ m s}^{-1}$ , similar to that shown in the observational studies of Heymsfield et al. (2001) and Guimond et al.

(2010) and the modeling study of Chen and Zhang (2013). Lower-tropospheric downdrafts are also evident at larger radii that are associated with the stratiform precipitation. The vertical vorticity field (Fig. 10d) shows the two vorticity cores seen in Fig. 6: one in the lower troposphere at the center extending up to 5 km, and the other in the midlevels at  $r = 50\text{--}60 \text{ km}$  extending from 4- to  $\sim 14\text{-km}$

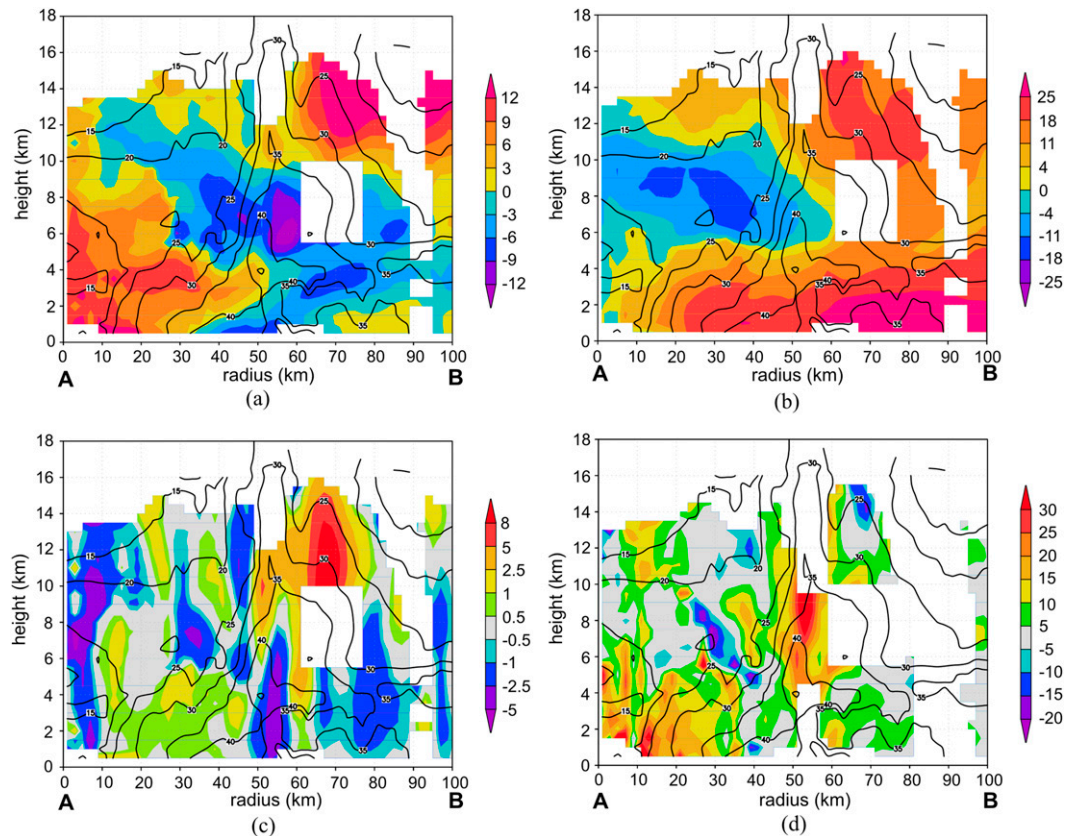


FIG. 10. (a) Cross section of the storm-relative  $u$  component of velocity (shaded,  $\text{m s}^{-1}$ ) and reflectivity (contour, dBZ) for line AB indicated in Fig. 6c. (b) As in (a), but for the  $v$  component of velocity (shaded,  $\text{m s}^{-1}$ ). (c) As in (a), but for vertical velocity (shaded,  $\text{m s}^{-1}$ ). (d) As in (a), but for vertical vorticity (shaded,  $\times 10^{-4} \text{ s}^{-1}$ ).

altitude (data coverage limitations at this altitude prevent a reliable determination of vortex depth). The vorticity cores do not appear to be connected; rather they appear to be distinct, separate cores.

From these analyses it is clear that the vertical structure of the vortex changes dramatically near the onset of RI. The CBs (and their associated mesoscale convective system) likely played a role in the transformation from an initially shallow low-level vortex circulation to a vertically penetrating vortex with a vertically aligned core of positive vorticity. Mechanisms potentially involved in the development of the vertically aligned vortex near the onset of RI are discussed further in section 5.

*b. Late stage: Convective bursts located inside radius of maximum winds*

By the time of the third mission, Earl was well into its RI period (cf. Fig. 1) and was now a category 1 hurricane of  $\sim 35 \text{ m s}^{-1}$ . The structure at this time consisted of a deep primary circulation and an RMW of  $\sim 50 \text{ km}$  that contracted to  $< 25 \text{ km}$  between the third and fifth missions (Fig. 5). Figure 11 shows the storm-relative flow

field and reflectivity at 2 km and CB locations from selected radial passes, along with concurrent lower fuselage reflectivity images, from each of the three missions during this stage. The bulk of the eyewall convection remains located left of the shear vector, even as the shear vector changes from being northeasterly to northwesterly from the third to the fifth flight. Additional banding features are evident outside the RMW, wrapping from the east side of the storm around to the south and west side. The radius of the peak eyewall convection, similar to the RMW, contracts during the three missions.

Figure 12 shows the center locations between 1- and 8-km altitude for the third through fifth missions. This calculation was done using a simplex method that identifies the location that maximizes the average tangential wind in an annulus centered at the RMW (Reasor et al. 2009, 2013; Reasor and Eastin 2012). The center locations shown in Fig. 12 are plotted relative to the shear vector, which changes from a value of  $\sim 5 \text{ m s}^{-1}$  from the northeast during the third flight to  $\sim 3 \text{ m s}^{-1}$  from the northwest during the fourth flight to  $\sim 5 \text{ m s}^{-1}$  from the northwest during the fifth flight (cf. Fig. 11, Table 1). During the

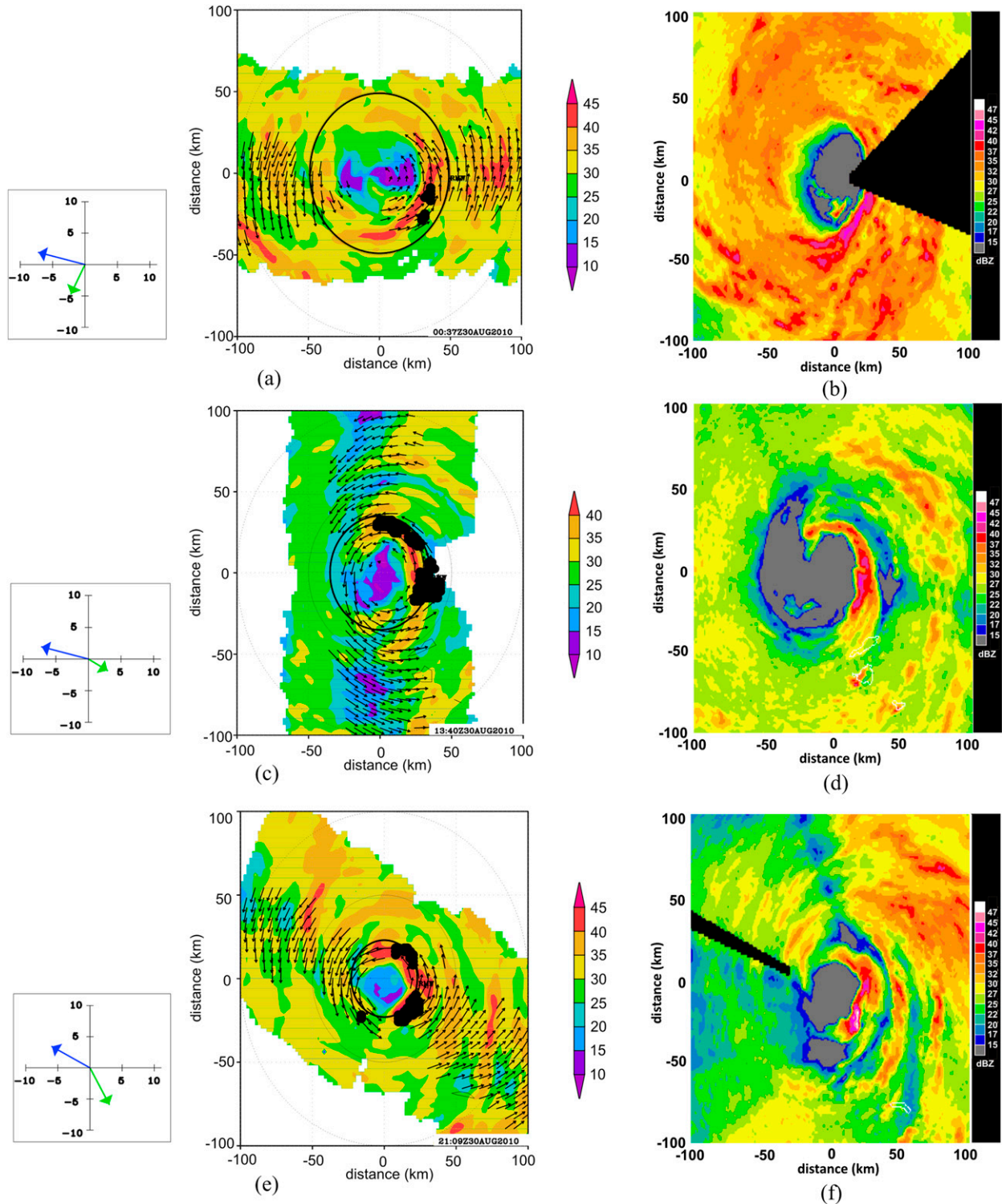


FIG. 11. (a) Reflectivity (shaded, dBZ) at 2-km altitude from the tail Doppler radar during individual radial pass through Earl centered at 0037 UTC 30 Aug. Vectors ( $\text{m s}^{-1}$ ) show storm-relative 8-km flow. Black dots denote locations of points flagged as convective bursts. RMW at 2-km altitude is indicated by a circle. (b) Storm-centered lower-fuselage reflectivity at  $\sim 3.5$  km from a single sweep at 0037 UTC. (c) As in (a), but for a pass centered at 1340 UTC 30 Aug. (d) As in (b), but for a sweep at 1338 UTC. (e) As in (a), but for a pass centered at 2109 UTC 30 Aug. (f) As in (b), but for a sweep at 2109 UTC and at  $\sim 2.5$ -km altitude. Domains in all images are 200 km on a side. Insets to the left of (a), (c), and (e) show SHIPS-derived shear vector (green arrow,  $\text{m s}^{-1}$ ) and storm motion vector (blue arrow,  $\text{m s}^{-1}$ ) for the 6-h time nearest to the mission.

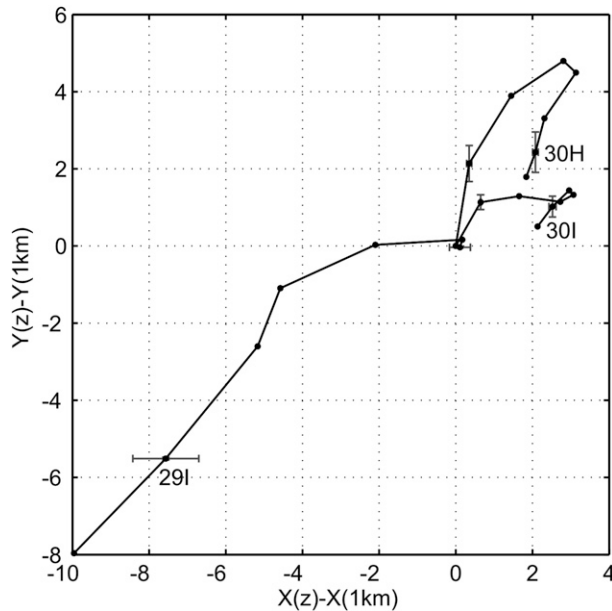


FIG. 12. The plot of center location using the simplex method (see text for details) for missions 100829I1, 100830H1, and 100830I1. The centers are plotted every 1 km from 1- to 8-km altitude (referenced to center at 1-km altitude). The 95% confidence intervals at 2 and 7 km are shown, based on an 11-member population of centers derived from using center-finding annulus widths from 3 to 13 km. The centers are rotated with the shear pointing to the right for all missions.

third flight the vortex shows a 2–7-km center displacement of  $\sim 10$  km toward the upshear-right quadrant. The magnitude of this displacement likely reflects the continued effect of the high shear ( $8\text{--}9\text{ m s}^{-1}$ ; Table 1) encountered by Earl during the first two flights. By the fourth flight, and continuing to the fifth flight, the vortex center shows a 2–7-km displacement on the order of 2 km toward the downshear-left quadrant. This orientation is generally consistent with that shown in rapidly intensifying Hurricane Guillermo (Reasor and Eastin 2012). Despite the alignment of the vortex during rapid intensification, there are still asymmetries in the flow field of the vortex. Figure 13 shows quadrant averages of storm-relative tangential and radial wind during the fourth mission. These quadrants are oriented relative to the vertical shear vector, which at this time was  $<5\text{ m s}^{-1}$  from the northwest (cf. Table 1, Figs. 2 and 11). The tangential wind is strongest on the downshear side and weakest in the upshear-right quadrant. The radial flow shows a deep inflow layer ( $>3$  km deep) on the downshear side, with the strongest inflow in the downshear-right quadrant. In the upshear-left quadrant there is low-level outflow and upper-level inflow, while in the upshear-right quadrant outflow predominates throughout the troposphere. This azimuthal variation of radial flow as a

function of shear (even in the presence of weak shear at this time) is generally consistent with the composite mean results of Reasor et al. (2013) and Zhang et al. (2013).

The distribution of CBs as a function of normalized radius is shown in Fig. 14 for both the early and late stages of Earl's RI. During the early stage the CBs are broadly distributed across radial bands inside  $r = 1.5 \times \text{RMW}$ , with a distinct peak inside  $r = 0.5 \times \text{RMW}$ . The increase in the RMW between the first and the second flight (i.e., from  $\sim 65$  to  $\sim 100$  km, cf. Fig. 5), may have aided in the development of Earl during this time, since an increase of the RMW would have placed more of the CBs inside the RMW. During the late stage the distribution of CBs becomes much more concentrated around the RMW, as the secondary circulation becomes better established and provides a stronger constraint on the radial location of deep convection. The peak CB activity remains inside the RMW (i.e., between the  $r = 0.75$  and  $1 \times \text{RMW}$  radial band), consistent with the composite results of intensifying hurricanes shown in R13. Dynamically this radial location is important because the peak diabatic heating associated with these CBs is located inside the RMW, where the vorticity and inertial stability are high (cf. Fig. 5) and the heating thus has a comparatively large impact on TC intensification (Shapiro and Willoughby 1982; Schubert and Hack 1982; Hack and Schubert 1986; Nolan et al. 2007; Vigh and Schubert 2009; Pendergrass and Willoughby 2009).

As mentioned above, the peak in the distribution of CBs inside the RMW at 2 km for Earl is consistent with intensifying hurricanes, as shown in R13. For steady-state hurricanes, by contrast, the radial distribution of CBs is characterized by a peak outside the RMW at 2 km. A key question to ask is why this relationship exists. One possible explanation is convergence in the boundary layer. Figure 15 shows radius–height plots of boundary layer axisymmetric tangential wind, radial wind, a gradient wind, and horizontal divergence (i.e.,  $V_r/r + \partial V_r/\partial r$ , where  $V_r$  is the radial flow), calculated from dropsondes from all aircraft from the 12-h period surrounding 0000 UTC 30 August. This matches one of the time periods examined in Montgomery et al. (2014), who performed a study of the boundary layer structure of Earl during its RI (see their Fig. 4b for a map of the dropsonde coverage). The tangential wind shows the RMW at around 40-km radius below 500-m altitude. Near-surface inflow values  $>14\text{ m s}^{-1}$  are seen at 75 km, or  $\sim 1.5 \times \text{RMW}$ , providing a significant inward advection of angular momentum. The tangential flow inside the RMW is highly supergradient from the surface to 2 km (Fig. 15c). The radial gradient of radial flow (Fig. 15d) shows that the strongest convergence is below 500 m and is located inside the RMW, with peak values

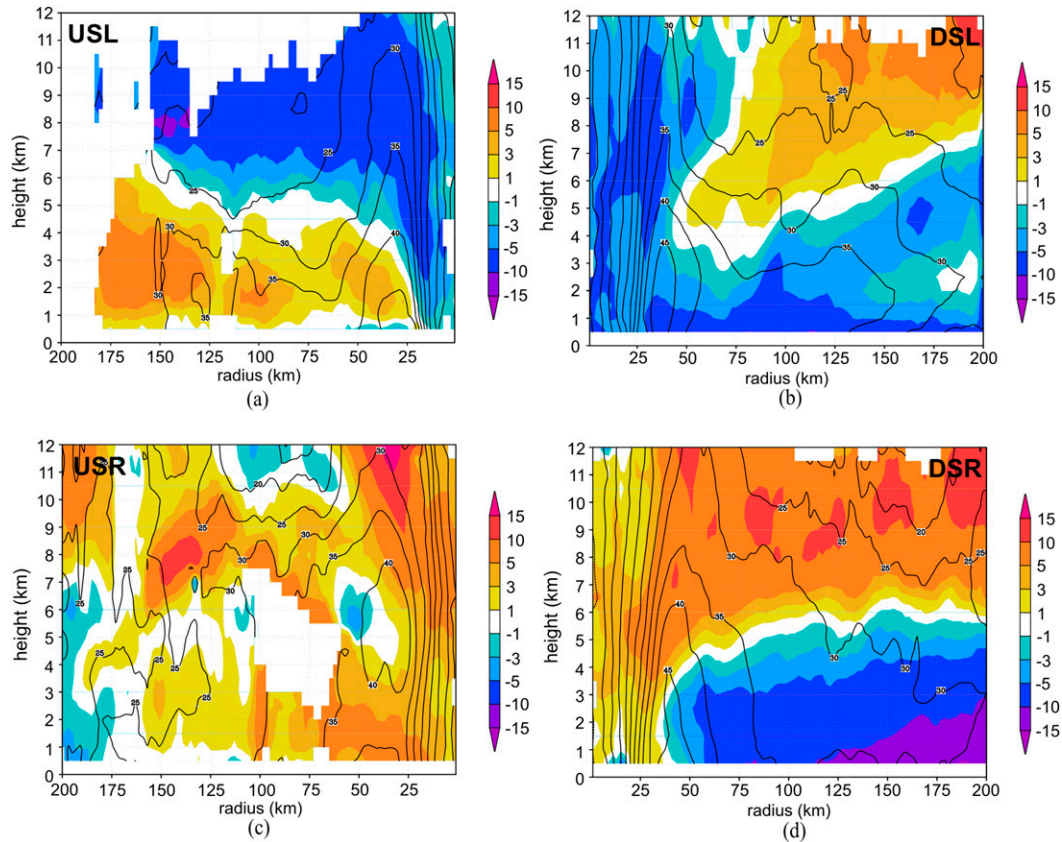


FIG. 13. Radius–height cross sections of storm-relative radial (shaded,  $\text{m s}^{-1}$ ) and tangential (contour,  $\text{m s}^{-1}$ ) flow for mission 100830H1. Fields are averaged within a quadrant relative to the SHIPS-derived 850–200-hPa shear vector: downshear-right quadrant (DSR), downshear-left quadrant (DSL), etc.

between  $0.5$  and  $1 \times \text{RMW}$ . This indicates that the low-level forcing for eyewall convection is inside the RMW for this case.

While Fig. 15 shows that boundary layer convergence was maximized inside the RMW for Earl, this mechanism cannot be definitively identified as one that governs the radial distribution of CBs, and hence distinguishes intensifying from steady-state hurricanes. What is needed is sufficient dropsonde coverage outside the RMW for a steady-state hurricane with similar characteristics to Earl to determine if convergence is maximized outside the RMW. Most WP-3D missions tend to drop sondes in the eyewall and turn points, and G-IV missions only drop sondes in the environment. Sondes are also dropped from other aircraft, such as the C-130, DC-8, and G-V, but these aircraft lack Doppler radar coverage spanning a broad area within the vortex. As a result, a dropsonde dataset with Doppler coverage of the eyewall and significant numbers of dropsondes in the  $1\text{--}3 \times \text{RMW}$  radial band are limited. In addition to the boundary layer convergence mechanism, there are other possible explanations for the difference in CB radial

distribution between intensifying and steady-state hurricanes that do not require a dense coverage of dropsondes outside the RMW. These explanations will be pursued in the next section.

## 5. Discussion

The results shown here have depicted the rapid intensification of Earl as occurring in two stages: the first stage, where the vortex became aligned in the presence of a vigorous convective burst, marking the onset of RI, and the second stage, where the vortex continued to rapidly intensify while convective bursts were located primarily inside the RMW. Each of the two stages described here raises questions about the role of convective- and vortex-scale processes in rapid intensification. These questions are discussed below.

### *a. Role of CBs and mesoscale convective system in vortex alignment and onset of RI*

In the case of the early stage, the primary questions pertain to the role that the convective burst and its

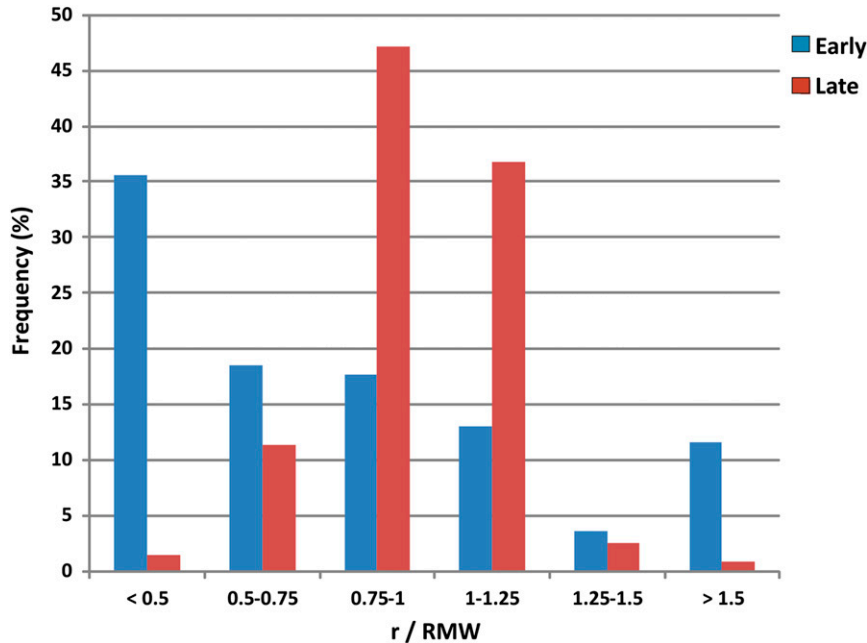


FIG. 14. Radial distribution of convective bursts (frequency, %) as a function of radius relative to 2-km RMW for early stage (blue) and late stage (red).

associated mesoscale convective system, play in the alignment of the vortex by the second mission (cf. Fig. 6). This alignment was an important step in the intensity evolution of Earl, as a vertically aligned vortex has a deeper, more well-developed secondary circulation that can effectively converge angular momentum surfaces and amplify the vortex (e.g., Ooyama 1982; Zehr 2003; Riemer et al. 2010). Without the benefit of radar observations prior to the first mission it is difficult to demonstrate definitively the origins of the midlevel vorticity maximum shown in Fig. 10. For a vortex initially extending through a deeper layer of the troposphere, differential advection of vorticity by the moderate shear flow could produce a displacement of the 8-km center from the 2-km center. The left-of-shear orientation of the observed displacement is consistent with prior idealized studies of vertically sheared tropical cyclones (e.g., Jones 1995, 2004; Wang and Holland 1996; Reasor et al. 2004). That the midlevel center appears to be tied to a region of persistent convection suggests a second, although not mutually exclusive, possibility in which the circulation there was caused by the CB and its convective system. Figure 10 indicates that the midlevel vorticity maximum may have resulted from, or at least been supported by, vortex stretching from the strong midlevel inflow and upper-level updrafts, as is commonly seen in midlevel mesoscale convective vortices (e.g., Johnston 1982; Bartels and Maddox 1991; Rogers and Fritsch 2001; Davis and Galarnau 2009).

Between the end of the first mission and the second mission the two distinct vorticity cores evolve into a single vertically aligned vortex. There were no radar observations during this 12-h period, so the midlevel vorticity maximum cannot be tracked in the time leading up to the aligned vortex. One possibility is that the midlevel vortex aligns with the low-level vortex following its precession upshear. It is also possible that the sustained organization of convection upshear left near the midlevel vorticity maximum promotes vertical development of the low-level vortex. A third possibility is that the midlevel vorticity maximum is transient and plays no role in the development of the aligned vortex; rather, the low-level vortex builds upward with time in a largely axisymmetric manner. Again, though, limited observations between the first and second missions prevent a definitive determination of this possibility. Higher time resolution data could shed light on these questions. Molinari and Vollaro (2010) documented the presence of an intense, small-scale vorticity maximum adjacent to a strong convective cell embedded within the broad circulation of Tropical Storm Gabrielle (2001), similar in many ways to that shown here. Even with Weather Surveillance Radar-1988 Doppler (WSR-88D) data at comparatively high time resolution ( $\sim 10$  min), however, they noted that the convective cell, adjacent small-scale vorticity maximum, and broader parent vortex evolved in a coupled manner and were not easily separable. High-resolution numerical model output could also yield insight into these interactions. Chen and

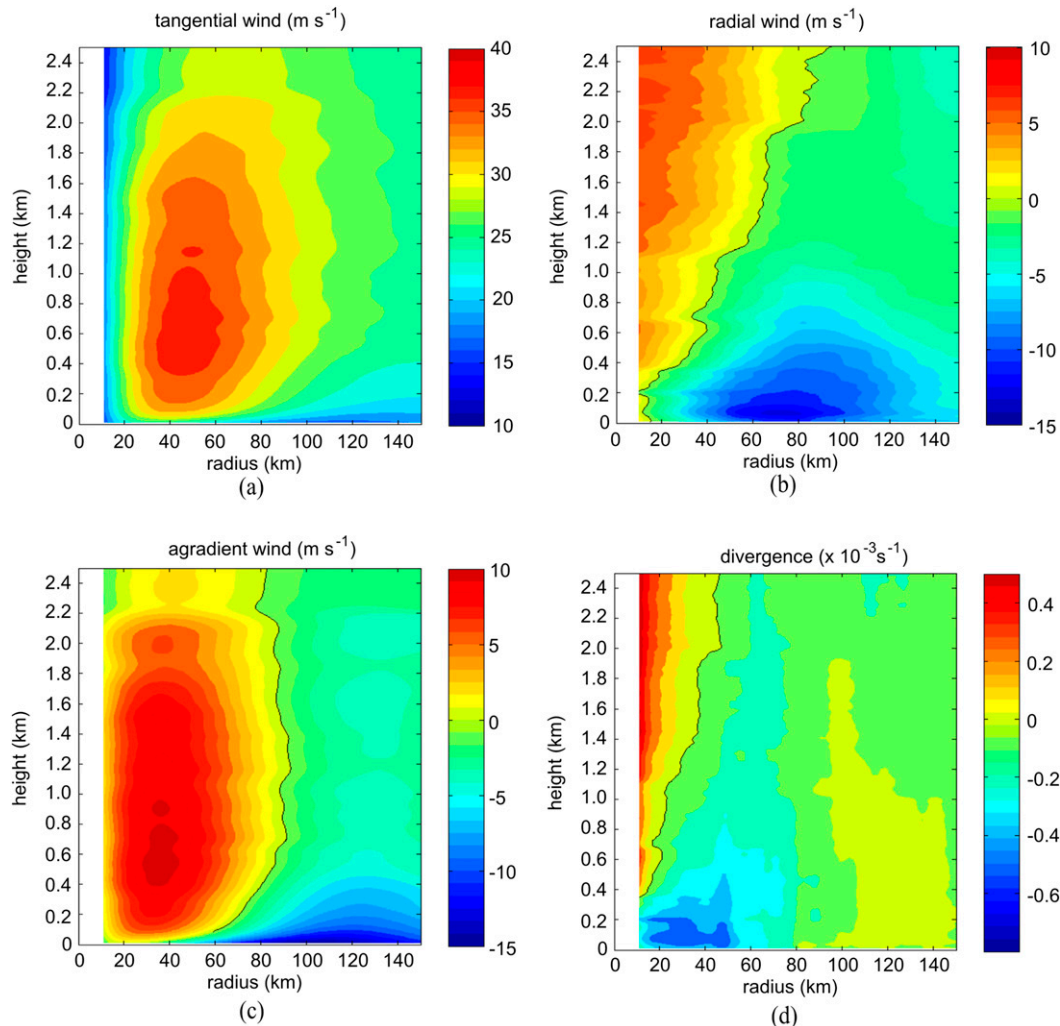


FIG. 15. (a) Radius–height plot of axisymmetric tangential wind (shaded,  $\text{m s}^{-1}$ ) from all dropsondes in a 12-h time window centered at 0000 UTC 30 Aug. (b) As in (a), but for axisymmetric radial flow (shaded,  $\text{m s}^{-1}$ ). (c) As in (a), but for agradient flow (shaded,  $\text{m s}^{-1}$ ). (d) As in (a), but for divergence (shaded,  $\times 10^{-3} \text{ s}^{-1}$ ). The black solid line denotes the zero contour.

Gopalakrishnan (2015) have produced a 3-km numerical model simulation of Earl’s RI that captures well the vortex displacement and subsequent alignment, so that is a dataset that could be further explored.

*b. Radial distribution of CBs: A comparison of an intensifying and steady-state case*

For the late stage, the primary question raised here was the processes that caused the CBs to be located inside the RMW for this rapidly intensifying hurricane. R13 offered some speculations of why intensifying hurricanes have the peak of the CB distribution inside the RMW, while steady-state hurricanes have the peak outside. One possibility was the radial location of low-level convergence. Boundary layer convergence within a radial band can be enhanced by the presence of CBs within that band, in

particular locally. However, there is less certainty of the degree to which this signal would be reflected in an azimuthally averaged sense. Furthermore, boundary layer theories for a well-developed steady-state TC involving no interaction with eyewall heating (e.g., Kepert 2001; Kepert and Wang 2001; Smith et al. 2008) indicate that boundary layer convergence tends to reach a maximum around the RMW, with the exact radial location dependent on the strength of the vortex and the drag coefficient used. Figure 15 showed that the peak radial convergence in the boundary layer for Earl is located inside the RMW. A related argument was advanced by Montgomery et al. (2014), Sanger et al. (2014), Montgomery and Smith (2012), and Smith et al. (2009), who examined radial inflow in the boundary layer and showed how it spins up the vortex by converging

absolute angular momentum at a rate that exceeds its dissipation to the ocean surface via friction. Convergence due to the radial gradient of radial inflow is maximized inside the RMW as the inflowing air slows and ascends, providing one possible forcing mechanism for CBs inside the RMW. Unfortunately, there is not a case of a steady-state hurricane with sufficient dropsonde coverage outside the RMW to test the hypothesis that steady-state cases would have their peak boundary layer convergence radially outward (including outside the RMW) compared with intensifying cases. This awaits additional cases with adequate dropsonde coverage, as well as numerical model studies.

Enhanced low-level convergence and organization of convection may also arise through the interaction of the vortex with vertically sheared environmental flow. The control that vertical shear forcing places on the azimuthal distribution of convection is evident near the RMW of Earl, with peak updrafts and precipitation in the downshear-left quadrant (see Figs. 6–7 and 11). One explanation for this convective asymmetry is based upon the dry, balanced dynamical evolution of vortex tilt under shear forcing (Jones 1995). In the moist context, balanced mesoscale lifting organizes convection (e.g., Davis et al. 2008). Another explanation for the shear-induced convective asymmetry relates convective organization to vorticity balance on the vortex scale (Willoughby et al. 1984; Bender 1997; Frank and Ritchie 2001). According to this argument, the tendency for vortex stretching to balance radial advection of vorticity requires low-level convergence and ascent in the quadrant where the low-level, storm-relative asymmetric flow approaches the RMW. The radial location of shear-forced mesoscale ascent has received less attention in the literature. In the context of midlatitude mesoscale convective vortices, Trier et al. (2000) examined the shear-induced development of convective asymmetry. They found that the location of thermodynamic destabilization was closely related to the region of maximum upward displacement in the lower troposphere, near the RMW in their simulations. In an idealized treatment of small-Rossby-number vortices in shear, Reasor et al. (2000) noted a dependence of the radial location of balanced asymmetric ascent on the radial profile of tangential wind. Further work extending the studies of Trier et al. (2000) and Reasor et al. (2000) to the TC may help elucidate how the radial location of shear-forced convective asymmetry depends on the shear and vortex structure.

Another explanation proposed in R13 was a reduced inertial stability outside the RMW in intensifying storms. This provides less resistance to radial displacements, resulting in a greater radial mass flux than steady-state cases. One way to test this hypothesis is to examine

differences in the inner-core structure for two cases: one that had CBs inside the 2-km RMW and intensified, and another that had CBs primarily outside the RMW and remained steady state. Figure 16 shows two such cases: the intensifying case is from the fourth mission in Earl, centered at  $\sim 1200$  UTC 30 August, and the steady-state case is Gustav, which was a  $\sim 42 \text{ m s}^{-1}$  hurricane at the time of the WP-3D mission centered at  $\sim 0000$  UTC 1 September 2008. Earl intensified  $10 \text{ m s}^{-1}$  in the 12-h time window centered on the mission, while Gustav's intensity did not change during this same window (not shown). Figure 16 shows 2-km wind speed and CB locations from a single pass, along with storm motion and 850–200-hPa vertical shear vectors, for the two missions. Both Gustav and Earl were tracking generally toward the west-northwest at  $\sim 7 \text{ m s}^{-1}$ . Earl was encountering northwesterly shear  $< 5 \text{ m s}^{-1}$ , while Gustav was encountering a southwesterly shear of  $\sim 6 \text{ m s}^{-1}$ . Both hurricanes had an RMW of  $\sim 35 \text{ km}$  at the time of their respective missions. Earl had most of its CB's inside the 2-km RMW, whereas Gustav had a significant number of CBs outside the RMW. This relationship is further illustrated in Fig. 16c, which shows the radial distribution of CBs for all radial passes comprising the Earl and Gustav missions shown in Figs. 16a,b. Earl shows a peak in CB distribution between  $0.75$  and  $1 \times \text{RMW}$ , consistent with Fig. 14, while Gustav shows a peak in CB distribution between  $1$  and  $1.25 \times \text{RMW}$ .

Figure 17 shows radius–height plots of axisymmetric inertial stability, tangential wind, and radial wind for the Earl and Gustav missions. The tangential wind and inertial stability fields inside the RMW are similar between the two storms below 6 km. Above that height the inertial stability is higher for Earl than Gustav. Outside the RMW, beginning at  $\sim 60\text{-km}$  radius (i.e.,  $\sim 2 \times \text{RMW}$ ), the tangential wind field is stronger and the inertial stability is higher in Gustav than Earl. A higher outer-core inertial stability can result in weaker, shallower inflow (Kepert 2001), reducing the convergence of angular momentum surfaces in an axisymmetric sense and weakening the “conventional spinup” mechanism (Ooyama 1982; Montgomery et al. 2014). The axisymmetric radial flow shown in Figs. 17c,d indicates that this relationship between inflow depth and outer-core inertial stability is generally followed, as the depth and magnitude of the inflow layer is larger for Earl than Gustav. Outside  $r = 100 \text{ km}$ , however, Earl's inflow remains deeper than Gustav despite comparable inertial stability values. This difference in inflow depth may be attributable to factors such as difference in coverage and strength of convective-scale downdrafts between the two storms (e.g., Powell 1990), though this examination is left for future work.

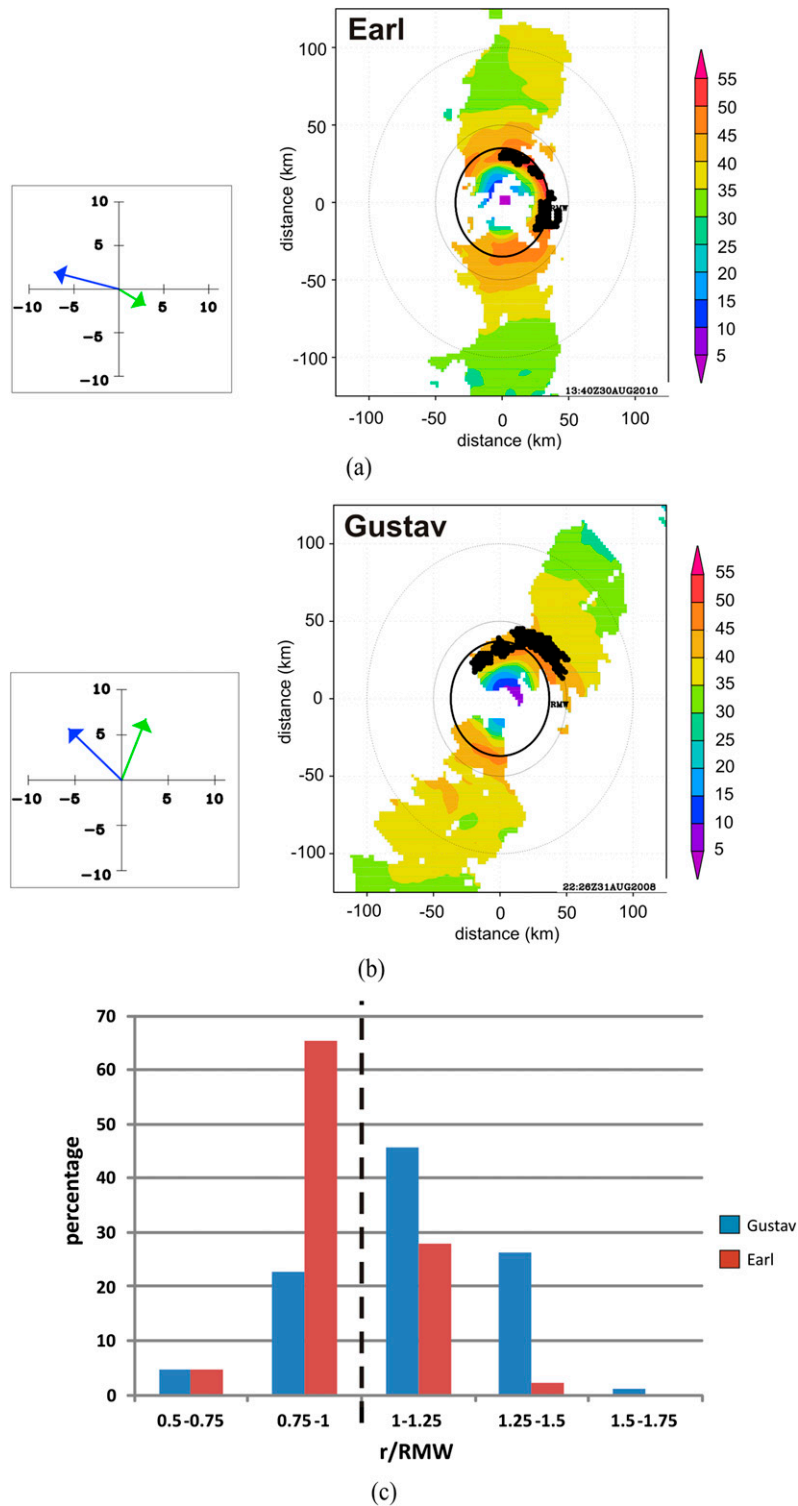


FIG. 16. (a) Storm-relative wind speed (shaded,  $\text{m s}^{-1}$ ) at 2-km altitude for a pass centered at 1340 UTC from mission 100830H1 in Hurricane Earl. (b) As in (a), but for a pass centered at 2226 UTC from mission 100831H1 in Hurricane Gustav. (c) Normalized radial distribution of convective bursts for all passes from the missions in Earl and Gustav from (a) and (b). The dashed line in (c) denotes the location of RMW. Insets to the left of (a) and (b) show the SHIPS-derived shear vector (green arrow,  $\text{m s}^{-1}$ ) and storm motion vector (blue arrow,  $\text{m s}^{-1}$ ) for the 6-h time nearest to the mission.

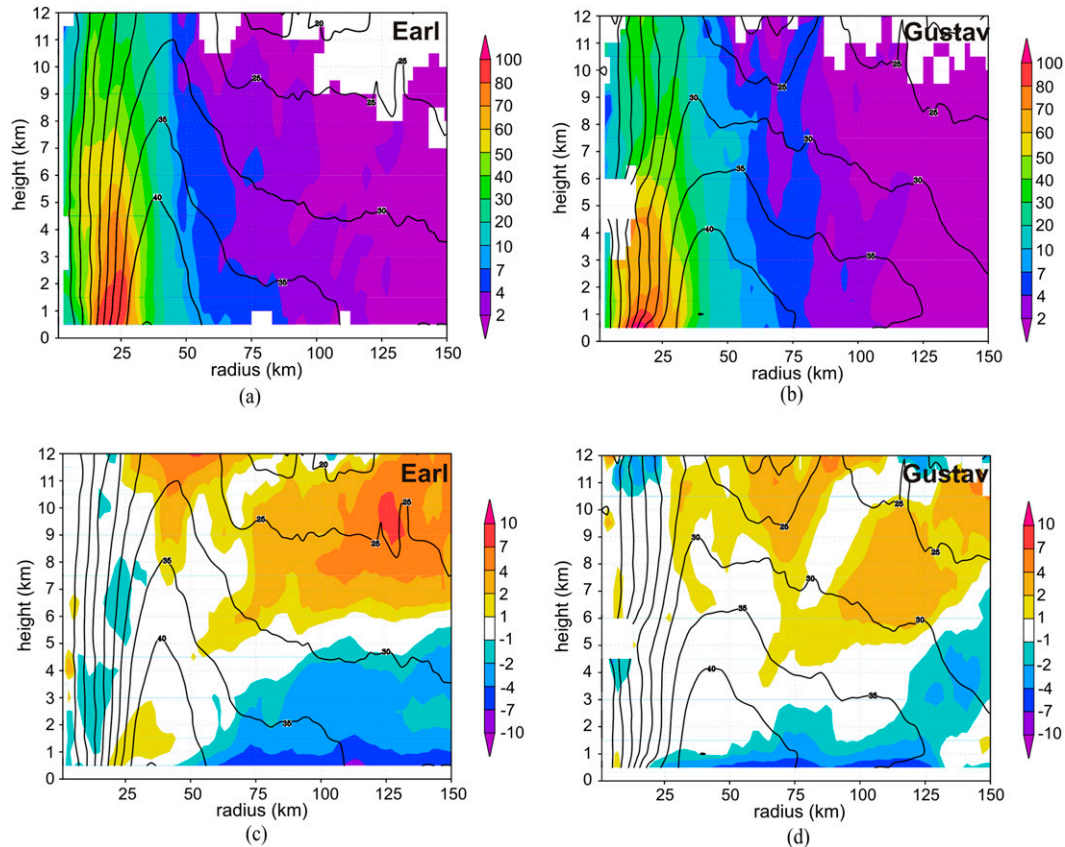


FIG. 17. (a) Radius–height plot of axisymmetric inertial stability ( $I^2$ , shaded,  $\times 10^{-7} \text{ s}^{-2}$ ) and tangential wind (contour,  $\text{m s}^{-1}$ ) for mission 100830H1 in Earl. (b) As in (a), but for mission 080831H1 in Gustav. (c) Radius–height plot of axisymmetric radial flow (shaded,  $\text{m s}^{-1}$ ) and tangential wind (contour,  $\text{m s}^{-1}$ ) for mission 100830H1 in Earl. (d) As in (c), but for mission 080831H1 in Gustav.

Since the relationship between CB radial location and RMW considers the RMW at 2-km altitude, whereas the criteria identifying CBs consider the vertical velocity and reflectivity above 8 km, CB locations based on this algorithm are also dependent on the slope of the updraft. The placement of a CB outside the 2-km RMW could simply reflect an updraft that is sloped, even if it had its origin in the low-level convergent region inside the RMW (cf. Fig. 15). Figure 18 shows comparisons of vertical velocity, inertial stability, and tangential wind averaged around the downshear side of Earl and Gustav. In addition, the angular momentum ( $M$ ) surfaces passing through the 2-km RMW and axes of peak updrafts are marked. The slope of the  $M$  surfaces is similar for both Earl and Gustav. Additionally, for both storms the peak updraft axis originates inside the 2-km RMW, consistent with the location of peak low-level convergence shown in Fig. 15 (for Earl). Above the low levels, though, the slope of the updraft axis differs. For Earl the updraft axis is nearly vertical, whereas for Gustav the updraft axis slopes outward between 5- and 8-km altitude. Above 8 km the

updraft axis for Gustav becomes nearly vertical again, where the updraft is the strongest. The angle between the updraft axis and  $M$  surface is large for Earl, while for Gustav the updraft axis is nearly parallel to the  $M$  surface (up to 8 km). An updraft axis, and by extension an axis of diabatic heating, that is more upright than the  $M$  surface results in a greater convergence of angular momentum and vortex spinup (Pendergrass and Willoughby 2009). Hazelton et al. (2015) found a similar relationship for intensifying and weakening hurricanes when they compared the slopes of reflectivity (which can be considered a proxy for updrafts) and  $M$  in the downshear-left and upshear-left quadrants. Another way to interpret this effect is to compare the location of the updraft axis with the local RMW (i.e., the RMW at the same height, rather than 2 km). For Earl the updraft axis remains inside the local RMW at all altitudes, while for Gustav the updraft axis crosses the local RMW at 7-km altitude and remains outside the RMW above. The updraft axis for Earl is thus located in a region of higher inertial stability throughout its ascent, compared with Gustav whose updraft axis

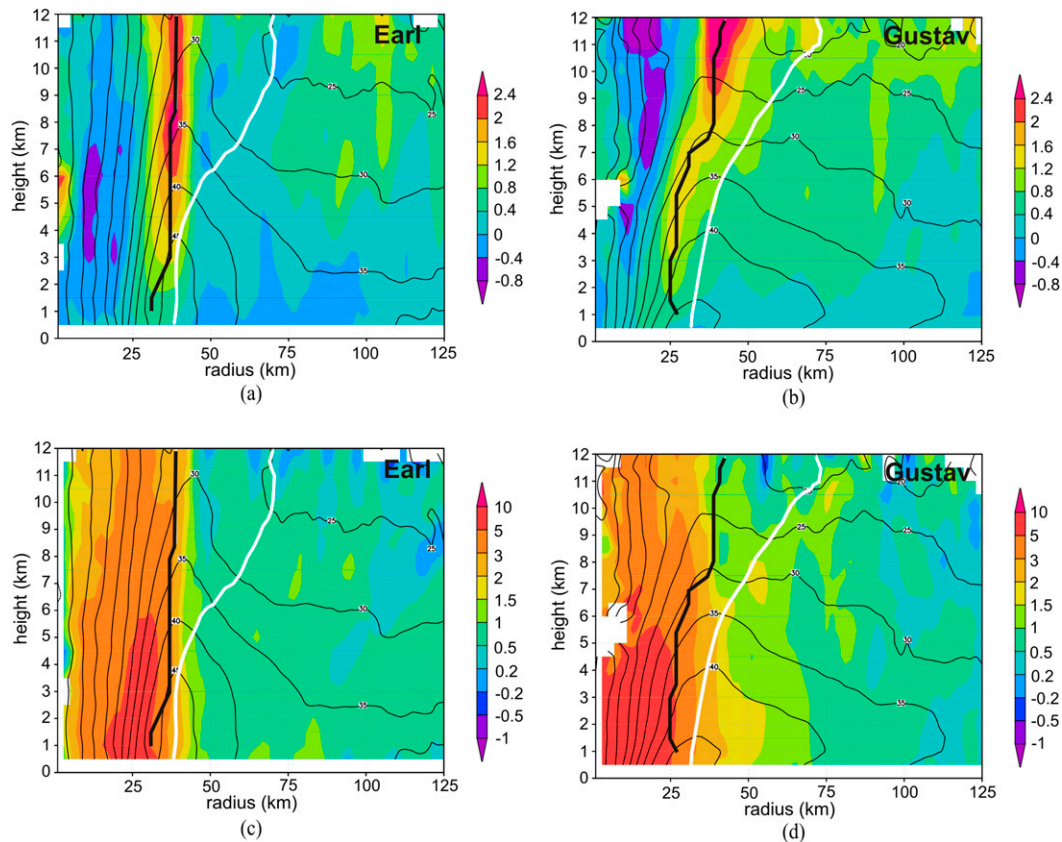


FIG. 18. (a) Radius–height plot of vertical velocity (shaded,  $\text{m s}^{-1}$ ) and tangential wind (contour,  $\text{m s}^{-1}$ ) on the downshear side for mission 100830H1 in Earl. (b) As in (a), but for mission 080831H1 in Gustav. (c) Radius–height plot of inertial stability ( $I^2$ , shaded,  $\times 10^{-7} \text{ s}^{-2}$ ) and tangential wind (contour,  $\text{m s}^{-1}$ ) on the downshear side for mission 100830H1 in Earl. (d) As in (c), but for mission 080831H1 in Gustav. In all figures the thick white solid line denotes angular momentum surface passing through 2-km RMW; the thick black line denotes the axis of peak updraft.

extends into a region of lower inertial stability (cf. Figs. 18b,d). As a result, the peak diabatic heating in Earl associated with these strong updrafts can more efficiently increase the kinetic energy of the storm for Earl than it can in Gustav.

The differences between Earl and Gustav highlighted above provide additional possibilities to explain why CBs appear to be preferentially located inside the 2-km RMW for intensifying hurricanes, whereas they are located outside the 2-km RMW for steady-state hurricanes. From the standpoint of updraft slope, the relevant question then becomes what causes updrafts to be more vertical in some cases and more sloped in others. One logical possibility is the buoyancy of the air flowing into the eyewall within the boundary layer. Figure 19 shows the relative humidity at 1-km altitude averaged from all dropsondes in Earl within a 12-h window centered on each of the five missions for the region spanning from the storm center to  $2 \times \text{RMW}$ . The inner-core boundary layer relative humidity steadily increases during this time, increasing from 92% during the

first flight to nearly 97% during the final flight, likely at least partially due to Earl's movement over warmer sea surface temperature (cf. Fig. 2c). Montgomery et al. (2014) also plotted the radial variation of equivalent potential temperature at 100- and 1500-m altitude for several different times for Earl. They show that the equivalent potential temperature at 1500 m is less than that at 100 m at all radii (out to 300 km) for both the first and third flights, suggesting a degree of convective instability in the boundary layer, especially when coupled with the increasing relative humidity shown in Fig. 19. Air with greater convective available potential energy would ascend more vigorously, departing from the local  $M$  surfaces and spinning up the vortex via the conventional method as discussed in Ooyama (1982). Unfortunately there is a lack of dropsonde coverage outside the RMW, and covering a deep layer of the troposphere, for cases spanning a spectrum of intensity change values, so a robust comparison between outer-core convective instability and intensity change cannot be performed.

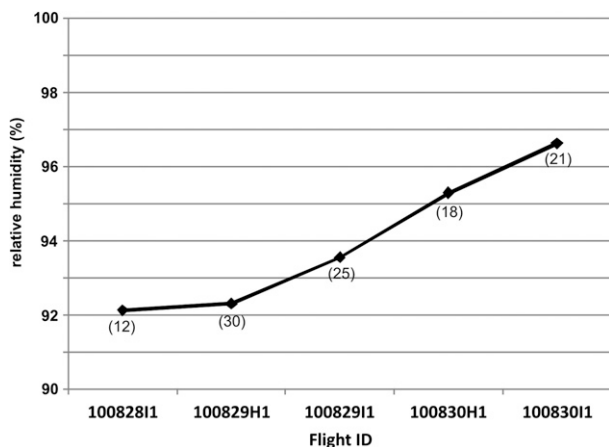


FIG. 19. Relative humidity (%) at 1-km altitude averaged from all dropsondes within a region spanning from the storm center to  $2 \times$  RMW for drops in a 12-h window centered on the flights indicated. The number in parentheses indicates the number of dropsondes composing each average.

## 6. Summary and conclusions

Using airborne observations from NOAA, NASA, and Air Force aircraft, the rapid intensification of Earl was documented. Earl's RI occurred in two stages. During the early stage, covering the first two WP-3D missions, the symmetric component of Earl was shallow, broad, and diffuse, as Earl was experiencing moderate northeasterly shear and had an asymmetric distribution of convection. During the first mission, the cyclonic circulation at 8 km was significantly displaced from the 2- and 5-km centers. There was a convective burst located on the east side of the storm that appeared to play a role in the development of a vertically coherent cyclonic circulation through the lowest 8-km depth. By the time of the second mission the vortex was aligned and extended over a deep layer, by which time rapid intensification had begun. During the late stage RI continued, as Earl intensified  $\sim 20 \text{ m s}^{-1}$  in the 24-h period composing this stage. The vortex remained generally aligned in the presence of weaker vertical shear, although azimuthal asymmetries in the flow field persisted that were characteristic of tropical cyclones in shear. Convective bursts were noted near the RMW during each of the three flights comprising this stage, with the majority of the CBs located just inside the RMW.

Several questions were raised from this analysis. In particular, the role of deep convection in Earl's RI was studied. For the early stage, when the displaced cyclonic circulation seen during the first mission became aligned by the time of the second mission, the role of the CB in this alignment was explored. Possible explanations for the alignment of the midlevel and low-level vortices were offered, including alignment of the low- and midlevel vortices following an upshear translation of the CB and

precession of the midlevel vortex, vertical development of low-level vorticity as the midlevel vortex organized deep convection, and the upward growth of low-level vorticity with no contribution from the midlevel vortex. For the late stage, possible mechanisms for the organization of CBs inside the RMW were proposed. These included a positioning of boundary layer convergence sufficiently inside the RMW to ensure that the initiation of deep convection remained inside the RMW, organization of convection within the region of mesoscale ascent forced by the vortex-shear interaction, inertial stability in the lower troposphere that was low enough to allow for a greater inward penetration of radial flow, and a slope of the updrafts from the vertical that was small enough compared with the angular momentum surfaces to produce a significant departure in the slopes of the updraft versus angular momentum surfaces.

While these are important questions to address in understanding the evolution of Earl's RI, and the role of deep convection in RI more broadly, limitations to the dataset preclude definitive answers from being found. In particular, a lack of temporal continuity prevents a determination of the processes that caused the midlevel circulation center to become aligned with the low-level center between the first and second WP-3D missions. Additionally, limited dropsonde observations outside the RMW, especially over a deep layer of the troposphere, prevent a determination of the radial profiles of boundary layer convergence and convective instability for the air approaching the eyewall. These fields are necessary to test the ideas pertaining to the radial location of CBs during the late stage of Earl's RI. Additional data needs to be collected that would focus on dropping a large number of sondes over a deep layer of the troposphere within and outside the RMW. Numerical model simulations of intensifying and steady-state hurricanes should also be examined, as they provide the temporal continuity and data coverage needed to diagnose the role of deep convection in rapid intensification.

*Acknowledgments.* The authors thank Hua Chen, John Kaplan, and two reviewers for their helpful comments on this manuscript; John Gamache, whose work on developing and implementing the automated Doppler quality control and synthesis routines, has been instrumental in performing this work; and Thiago Quirino, who provided the GFS analysis grids shown here. Our thanks also go to the staff of NOAA's Aircraft Operations Center for skillfully and reliably collecting this data. Funding for this work was provided by NOAA base funds through the NOAA Hurricane Forecast Improvement Project (HFIP) and the NASA Hurricane and Severe Storm Sentinel (HS3) Project NNG11HG001.

## REFERENCES

- Bartels, D. L., and R. A. Maddox, 1991: Midlevel cyclonic vortices generated by mesoscale convective systems. *Mon. Wea. Rev.*, **119**, 104–118, doi:10.1175/1520-0493(1991)119<0104:MCVGBM>2.0.CO;2.
- Bender, M. A., 1997: The effect of relative flow on the asymmetric structure in the interior of hurricanes. *J. Atmos. Sci.*, **54**, 703–724, doi:10.1175/1520-0469(1997)054<0703:TEORFO>2.0.CO;2.
- Black, M. L., R. W. Burpee, and F. D. Marks Jr., 1996: Vertical motion characteristics of tropical cyclones determined with airborne Doppler radial velocities. *J. Atmos. Sci.*, **53**, 1887–1909, doi:10.1175/1520-0469(1996)053<1887:VMCOTC>2.0.CO;2.
- , J. F. Gamache, F. D. Marks, C. E. Samsury, and H. E. Willoughby, 2002: Eastern Pacific Hurricanes Jimena of 1991 and Olivia of 1994: The effect of vertical shear on structure and intensity. *Mon. Wea. Rev.*, **130**, 2291–2312, doi:10.1175/1520-0493(2002)130<2291:EPHJOA>2.0.CO;2.
- Braun, S. A., and Coauthors, 2013: NASA's Genesis and Rapid Intensification Processes (GRIP) Field Experiment. *Bull. Amer. Meteor. Soc.*, **94**, 345–363, doi:10.1175/BAMS-D-11-00232.1.
- Cangialosi, J. P., 2010: Tropical Cyclone Report: Hurricane Earl. National Hurricane Center Tropical Cyclone Rep. AL072010, 29 pp. [Available online at [http://www.nhc.noaa.gov/pdf/TCR-AL072010\\_Earl.pdf](http://www.nhc.noaa.gov/pdf/TCR-AL072010_Earl.pdf).]
- Cecil, D. J., E. J. Zipsper, and S. W. Nesbitt, 2002: Reflectivity, ice scattering, and lightning characteristics of hurricane eyewalls and rainbands. Part I: Quantitative description. *Mon. Wea. Rev.*, **130**, 769–784, doi:10.1175/1520-0493(2002)130<0769:RISALC>2.0.CO;2.
- Chen, H., and D. L. Zhang, 2013: On the rapid intensification of Hurricane Wilma (2005). Part II: Convective bursts and the upper-level warm core. *J. Atmos. Sci.*, **70**, 146–162, doi:10.1175/JAS-D-12-062.1.
- , and S. G. Gopalakrishnan, 2015: A study on the asymmetric rapid intensification of Hurricane Earl (2010) using the HWRF system. *J. Atmos. Sci.*, in press.
- Cram, T. A., J. Persing, M. T. Montgomery, and S. A. Braun, 2007: A Lagrangian trajectory view on transport and mixing processes between the eye, eyewall, and environment using a high-resolution simulation of Hurricane Bonnie (1998). *J. Atmos. Sci.*, **64**, 1835–1856, doi:10.1175/JAS3921.1.
- Davis, C. A., and T. J. Galarneau, 2009: The vertical structure of mesoscale convective vortices. *J. Atmos. Sci.*, **66**, 686–704, doi:10.1175/2008JAS2819.1.
- , S. C. Jones, and M. Riemer, 2008: Hurricane vortex dynamics during Atlantic extratropical transition. *J. Atmos. Sci.*, **65**, 714–736, doi:10.1175/2007JAS2488.1.
- DeHart, J. C., R. A. Houze Jr., and R. F. Rogers, 2014: Quadrant distribution of tropical cyclone inner-core kinematics in relation to environmental shear. *J. Atmos. Sci.*, **71**, 2713–2732, doi:10.1175/JAS-D-13-0298.1.
- DeMaria, M., M. Mainelli, L. K. Shay, J. A. Knaff, and J. Kaplan, 2005: Further improvements to the Statistical Hurricane Intensity Prediction Scheme (SHIPS). *Wea. Forecasting*, **20**, 531–543, doi:10.1175/WAF862.1.
- , C. R. Sampson, J. A. Knaff, and K. D. Musgrave, 2014: Is tropical cyclone intensity guidance improving? *Bull. Amer. Meteor. Soc.*, **95**, 387–398, doi:10.1175/BAMS-D-12-00240.1.
- Didlake, A. C., and R. A. Houze, 2011: Kinematics of the secondary eyewall observed in Hurricane Rita (2005). *J. Atmos. Sci.*, **68**, 1620–1636, doi:10.1175/2011JAS3715.1.
- Dunkerton, T. J., M. T. Montgomery, and Z. Wang, 2009: Tropical cyclogenesis in a tropical wave critical layer: Easterly waves. *Atmos. Chem. Phys.*, **9**, 5587–5646, doi:10.5194/acp-9-5587-2009.
- Frank, W. M., and E. A. Ritchie, 2001: Effects of vertical wind shear on the intensity and structure of numerically simulated hurricanes. *Mon. Wea. Rev.*, **129**, 2249–2269, doi:10.1175/1520-0493(2001)129<2249:EOVWSO>2.0.CO;2.
- Franklin, J. L., M. L. Black, and K. Valde, 2003: GPS dropwindsonde wind profiles in hurricanes and their operational implications. *Wea. Forecasting*, **18**, 32–44, doi:10.1175/1520-0434(2003)018<0032:GDWPIH>2.0.CO;2.
- Gamache, J. F., 1997: Evaluation of a fully three-dimensional variational Doppler analysis technique. Preprints, *28th Conf. on Radar Meteorology*, Austin, TX, Amer. Meteor. Soc., 422–423.
- Gentry, R. C., T. T. Fujita, and R. C. Sheets, 1970: Aircraft, spacecraft, satellite, and radar observations of Hurricane Gladys, 1968. *J. Appl. Meteor.*, **9**, 837–850, doi:10.1175/1520-0450(1970)009<0837:ASSARO>2.0.CO;2.
- Guimond, S. R., G. M. Heymsfield, and F. J. Turk, 2010: Multiscale observations of Hurricane Dennis (2005): The effects of hot towers on rapid intensification. *J. Atmos. Sci.*, **67**, 633–654, doi:10.1175/2009JAS3119.1.
- Hack, J. J., and W. H. Schubert, 1986: Nonlinear response of atmospheric vortices to heating by organized cumulus convection. *J. Atmos. Sci.*, **43**, 1559–1573, doi:10.1175/1520-0469(1986)043<1559:NROAVT>2.0.CO;2.
- Hazelton, A. T., and R. E. Hart, 2013: Hurricane eyewall slope as determined from airborne radar reflectivity data: Composites and case studies. *Wea. Forecasting*, **28**, 368–386, doi:10.1175/WAF-D-12-00037.1.
- , R. F. Rogers, and R. E. Hart, 2015: Shear-relative asymmetries in tropical cyclone eyewall slope. *Mon. Wea. Rev.*, in press.
- Hendricks, E. A., M. T. Montgomery, and C. A. Davis, 2004: The role of “vortical” hot towers in the formation of Tropical Cyclone Diana (1984). *J. Atmos. Sci.*, **61**, 1209–1232, doi:10.1175/1520-0469(2004)061<1209:TROVHT>2.0.CO;2.
- , M. S. Peng, B. Fu, and T. Li, 2010: Quantifying environmental control on tropical cyclone intensity change. *Mon. Wea. Rev.*, **138**, 3243–3271, doi:10.1175/2010MWR3185.1.
- Hennon, P. A., 2006: The role of the ocean in convective burst initiation: Implications for tropical cyclone intensification. Ph.D. dissertation, The Ohio State University, 185 pp.
- Heymsfield, G. M., J. B. Halverson, J. Simpson, L. Tian, and T. P. Bui, 2001: ER-2 Doppler radar investigations of the eyewall of Hurricane Bonnie during the Convection and Moisture Experiment-3. *J. Appl. Meteor.*, **40**, 1310–1330, doi:10.1175/1520-0450(2001)040<1310:EDRIOT>2.0.CO;2.
- , L. Tian, A. J. Heymsfield, L. Li, and S. Guimond, 2010: Characteristics of deep tropical and subtropical convection from nadir-viewing high-altitude airborne Doppler radar. *J. Atmos. Sci.*, **67**, 285–308, doi:10.1175/2009JAS3132.1.
- Hock, T. F., and J. L. Franklin, 1999: The NCAR GPS dropwindsonde. *Bull. Amer. Meteor. Soc.*, **80**, 407–420, doi:10.1175/1520-0477(1999)080<0407:TNGD>2.0.CO;2.
- Houze, R. A., Jr., W.-C. Lee, and M. M. Bell, 2009: Convective contribution to the genesis of Hurricane Ophelia (2005). *Mon. Wea. Rev.*, **137**, 2778–2800, doi:10.1175/2009MWR2727.1.
- Jiang, H., 2012: The relationship between tropical cyclone intensity change and the strength of inner-core convection. *Mon. Wea. Rev.*, **140**, 1164–1176, doi:10.1175/MWR-D-11-00134.1.
- Johnston, E. C., 1982: Mesoscale vorticity centers induced by mesoscale convective complexes. Preprints, *Ninth Conf. on Weather*

- Forecasting and Analysis*, Seattle, WA, Amer. Meteor. Soc., 196–200.
- Jones, S. C., 1995: The evolution of vortices in vertical shear. I: Initially barotropic vortices. *Quart. J. Roy. Meteor. Soc.*, **121**, 821–851, doi:10.1002/qj.49712152406.
- , 2004: On the ability of dry tropical-cyclone-like vortices to withstand vertical shear. *J. Atmos. Sci.*, **61**, 114–119, doi:10.1175/1520-0469(2004)061<0114:OTAODT>2.0.CO;2.
- Kaplan, J., M. DeMaria, and J. A. Knaff, 2010: A revised tropical cyclone rapid intensification index for the Atlantic and eastern North Pacific basins. *Wea. Forecasting*, **25**, 220–241, doi:10.1175/2009WAF2222280.1.
- Kelley, O. A., J. Stout, and J. B. Halverson, 2004: Tall precipitation cells in tropical cyclone eyewalls are associated with tropical cyclone intensification. *Geophys. Res. Lett.*, **31**, L24112, doi:10.1029/2004GL021616.
- Kepert, J. D., 2001: The dynamics of boundary layer jets within the tropical cyclone core. Part I: Linear theory. *J. Atmos. Sci.*, **58**, 2469–2484, doi:10.1175/1520-0469(2001)058<2469:TDOBLJ>2.0.CO;2.
- , and Y. Wang, 2001: The dynamics of boundary layer jets within the tropical cyclone core. Part II: Nonlinear enhancement. *J. Atmos. Sci.*, **58**, 2485–2501, doi:10.1175/1520-0469(2001)058<2485:TDOBLJ>2.0.CO;2.
- Kieper, M. E., and H. Jiang, 2012: Predicting tropical cyclone rapid intensification using the 37 GHz ring pattern identified from passive microwave measurements. *Geophys. Res. Lett.*, **39**, L13804, doi:10.1029/2012GL052115.
- Kossin, J. P., and M. D. Eastin, 2001: Two distinct regimes in the kinematic and thermodynamic structure of the hurricane eye and eyewall. *J. Atmos. Sci.*, **58**, 1079–1090, doi:10.1175/1520-0469(2001)058<1079:TDRITK>2.0.CO;2.
- , and W. H. Schubert, 2001: Mesovortices, polygonal flow patterns, and rapid pressure falls in hurricane-like vortices. *J. Atmos. Sci.*, **58**, 2196–2209, doi:10.1175/1520-0469(2001)058<2196:MPFPAR>2.0.CO;2.
- Mallen, K. J., M. T. Montgomery, and B. Wang, 2005: Reexamining the near-core radial structure of the tropical cyclone primary circulation: Implications for vortex resiliency. *J. Atmos. Sci.*, **62**, 408–425, doi:10.1175/JAS-3377.1.
- Marks, F. D., Jr., and L. K. Shay, 1998: Landfalling tropical cyclones: Forecast problems and associated research opportunities. *Bull. Amer. Meteor. Soc.*, **79**, 305–323, doi:10.1175/1520-0477(1998)079<0305:LTCFPA>2.0.CO;2.
- Molinari, J., and D. Vollaro, 2010: Rapid intensification of a sheared tropical storm. *Mon. Wea. Rev.*, **138**, 3869–3885, doi:10.1175/2010MWR3378.1.
- Montgomery, M. T., and R. K. Smith, 2012: Paradigms for tropical-cyclone intensification. *Trop. Cyc. Res. Rep.*, **1**, 1–29.
- , V. A. Vladimirov, and P. V. Denissenko, 2002: An experimental study on hurricane mesovortices. *J. Fluid Mech.*, **471**, 1–32, doi:10.1017/S0022112002001647.
- , M. Nicholls, T. Cram, and A. Saunders, 2006: A “vortical” hot tower route to tropical cyclogenesis. *J. Atmos. Sci.*, **63**, 355–386, doi:10.1175/JAS3604.1.
- , and Coauthors, 2012: The Pre-Depression Investigation of Cloud-Systems in the Tropics (PREDICT) Experiment: Scientific basis, new analysis tools, and some first results. *Bull. Amer. Meteor. Soc.*, **93**, 153–172, doi:10.1175/BAMS-D-11-00046.1.
- , J. A. Zhang, and R. K. Smith, 2014: An analysis of the observed low-level structure of rapidly intensifying and mature Hurricane Earl (2010). *Quart. J. Roy. Meteor. Soc.*, **140**, 2132–2146, doi:10.1002/qj.2283.
- Nguyen, C. M., M. J. Reeder, N. E. Davidson, R. K. Smith, and M. T. Montgomery, 2011: Inner-core vacillation cycles during the intensification of Hurricane Katrina. *Quart. J. Roy. Meteor. Soc.*, **137**, 829–844, doi:10.1002/qj.823.
- Nguyen, L. T., and J. Molinari, 2012: Rapid intensification of a sheared, fast-moving hurricane over the Gulf Stream. *Mon. Wea. Rev.*, **140**, 3361–3378, doi:10.1175/MWR-D-11-00293.1.
- Nolan, D. S., and L. D. Grasso, 2003: Nonhydrostatic, three-dimensional perturbations to balanced, hurricane-like vortices. Part II: Symmetric response and nonlinear simulations. *J. Atmos. Sci.*, **60**, 2717–2745, doi:10.1175/1520-0469(2003)060<2717:NTPTBH>2.0.CO;2.
- , Y. Moon, and D. P. Stern, 2007: Tropical cyclone intensification from asymmetric convection: Energetics and efficiency. *J. Atmos. Sci.*, **64**, 3377–3405, doi:10.1175/JAS3988.1.
- Ooyama, K., 1969: Numerical simulation of the life cycle of tropical cyclones. *J. Atmos. Sci.*, **26**, 3–40, doi:10.1175/1520-0469(1969)026<0003:NSOTLC>2.0.CO;2.
- , 1982: Conceptual evolution of the theory and modeling of the tropical cyclone. *J. Meteor. Soc. Japan*, **60**, 369–380.
- Pendergrass, A. G., and H. E. Willoughby, 2009: Diabatically induced secondary flows in tropical cyclones. Part I: Quasi-steady forcing. *Mon. Wea. Rev.*, **137**, 805–821, doi:10.1175/2008MWR2657.1.
- Persing, J., and M. T. Montgomery, 2003: Hurricane superintensity. *J. Atmos. Sci.*, **60**, 2349–2371, doi:10.1175/1520-0469(2003)060<2349:HS>2.0.CO;2.
- Powell, M. D., 1990: Boundary layer structure and dynamics in outer hurricane rainbands. Part II: Downdraft modification and mixed layer recovery. *Mon. Wea. Rev.*, **118**, 918–938, doi:10.1175/1520-0493(1990)118<0918:BLSADI>2.0.CO;2.
- Reasor, P. D., and M. T. Montgomery, 2001: Three-dimensional alignment and corotation of weak, TC-like vortices via linear vortex Rossby waves. *J. Atmos. Sci.*, **58**, 2306–2330, doi:10.1175/1520-0469(2001)058<2306:TDAACO>2.0.CO;2.
- , and M. D. Eastin, 2012: Rapidly intensifying Hurricane Guillermo (1997). Part II: Resilience in shear. *Mon. Wea. Rev.*, **140**, 425–444, doi:10.1175/MWR-D-11-00080.1.
- , M. T. Montgomery, F. D. Marks Jr., and J. F. Gamache, 2000: Low-wavenumber structure and evolution of the hurricane inner core observed by airborne dual-Doppler radar. *Mon. Wea. Rev.*, **128**, 1653–1680, doi:10.1175/1520-0493(2000)128<1653:LWSAEO>2.0.CO;2.
- , —, and L. D. Grasso, 2004: A new look at the problem of tropical cyclones in vertical shear flow: Vortex resiliency. *J. Atmos. Sci.*, **61**, 3–22, doi:10.1175/1520-0469(2004)061<0003:ANLATP>2.0.CO;2.
- , M. D. Eastin, and J. F. Gamache, 2009: Rapidly intensifying Hurricane Guillermo (1997). Part I: Low-wavenumber structure and evolution. *Mon. Wea. Rev.*, **137**, 603–631, doi:10.1175/2008MWR2487.1.
- , R. F. Rogers, and S. Lorsolo, 2013: Environmental flow impacts on tropical cyclone structure diagnosed from airborne Doppler radar composites. *Mon. Wea. Rev.*, **141**, 2949–2969, doi:10.1175/MWR-D-12-00334.1.
- Riemer, M., M. T. Montgomery, and M. E. Nicholls, 2010: A new paradigm for intensity modification of tropical cyclones: Thermodynamic impact of vertical wind shear on the inflow layer. *Atmos. Chem. Phys.*, **10**, 3163–3188, doi:10.5194/acp-10-3163-2010.
- Rodgers, E. B., W. S. Olson, V. M. Karyampudi, and H. F. Pierce, 1998: Satellite-derived latent heating distribution and environmental influences in Hurricane Opal (1995). *Mon. Wea.*

- Rev.*, **126**, 1229–1247, doi:10.1175/1520-0493(1998)126<1229:SDLHDA>2.0.CO;2.
- Rogers, R. F., 2010: Convective-scale structure and evolution during a high-resolution simulation of tropical cyclone rapid intensification. *J. Atmos. Sci.*, **67**, 44–70, doi:10.1175/2009JAS3122.1.
- , and J. M. Fritsch, 2001: Surface cyclogenesis from convectively driven amplification of midlevel mesoscale convective vortices. *Mon. Wea. Rev.*, **129**, 605–637, doi:10.1175/1520-0493(2001)129<0605:SCFCDA>2.0.CO;2.
- , S. S. Chen, J. Tenerelli, and H. E. Willoughby, 2003: A numerical study of the impact of vertical shear on the distribution of rainfall in Hurricane Bonnie (1998). *Mon. Wea. Rev.*, **131**, 1577–1599, doi:10.1175//2546.1.
- , and Coauthors, 2006: The Intensity Forecasting Experiment: A NOAA multiyear field program for improving tropical cyclone intensity forecasts. *Bull. Amer. Meteor. Soc.*, **87**, 1523–1537, doi:10.1175/BAMS-87-11-1523.
- , S. Lorsolo, P. D. Reasor, J. Gamache, and F. D. Marks Jr., 2012: Multiscale analysis of tropical cyclone kinematic structure from airborne Doppler radar composites. *Mon. Wea. Rev.*, **140**, 77–99, doi:10.1175/MWR-D-10-05075.1.
- , P. D. Reasor, and S. Lorsolo, 2013a: Airborne Doppler observations of the inner-core structural differences between intensifying and steady-state tropical cyclones. *Mon. Wea. Rev.*, **141**, 2970–2991, doi:10.1175/MWR-D-12-00357.1.
- , and Coauthors, 2013b: NOAA's Hurricane Intensity Forecasting Experiment (IFEX): A progress report. *Bull. Amer. Meteor. Soc.*, **94**, 859–882, doi:10.1175/BAMS-D-12-00089.1.
- Sanger, N. T., M. T. Montgomery, R. K. Smith, and M. M. Bell, 2014: An observational study of tropical cyclone spinup in Supertyphoon Jangmi (2008) from 24 to 27 September. *Mon. Wea. Rev.*, **142**, 3–28, doi:10.1175/MWR-D-12-00306.1.
- Schubert, W. H., and J. J. Hack, 1982: Inertial stability and tropical cyclone development. *J. Atmos. Sci.*, **39**, 1687–1697, doi:10.1175/1520-0469(1982)039<1687:ISATCD>2.0.CO;2.
- , M. T. Montgomery, R. K. Taft, T. A. Guinn, S. R. Fulton, J. P. Kossin, and J. P. Edwards, 1999: Polygonal eyewalls, asymmetric eye contraction, and potential vorticity mixing in hurricanes. *J. Atmos. Sci.*, **56**, 1197–1223, doi:10.1175/1520-0469(1999)056<1197:PEAECA>2.0.CO;2.
- Shapiro, L. J., and H. E. Willoughby, 1982: The response of balanced hurricanes to local sources of heat and momentum. *J. Atmos. Sci.*, **39**, 378–394, doi:10.1175/1520-0469(1982)039<0378:TROBHT>2.0.CO;2.
- Smith, R. K., M. T. Montgomery, and S. Vogl, 2008: A critique of Emanuel's hurricane model and potential intensity theory. *Quart. J. Roy. Meteor. Soc.*, **134**, 551–561, doi:10.1002/qj.241.
- , —, and N. V. Sang, 2009: Tropical cyclone spin up revisited. *Quart. J. Roy. Meteor. Soc.*, **135**, 1321–1335, doi:10.1002/qj.428.
- Squires, K., and S. Businger, 2008: The morphology of eyewall lightning outbreaks in two category 5 hurricanes. *Mon. Wea. Rev.*, **136**, 1706–1726, doi:10.1175/2007MWR2150.1.
- Stern, D. P., and D. S. Nolan, 2009: Reexamining the vertical structure of tangential winds in tropical cyclones: Observations and theory. *J. Atmos. Sci.*, **66**, 3579–3600, doi:10.1175/2009JAS2916.1.
- , and —, 2011: On the vertical decay rate of the maximum tangential winds in tropical cyclones. *J. Atmos. Sci.*, **68**, 2073–2094, doi:10.1175/2011JAS3682.1.
- Trier, S. B., C. A. Davis, and W. C. Skamarock, 2000: Long-lived mesoconvective vortices and their environment. Part II: Induced thermodynamic destabilization in idealized simulations. *Mon. Wea. Rev.*, **128**, 3396–3412, doi:10.1175/1520-0493(2000)128<3396:LLMVAT>2.0.CO;2.
- Uhlhorn, E. W., B. W. Klotz, T. Vukicevic, P. D. Reasor, and R. F. Rogers, 2014: Observed hurricane wind speed asymmetries and relationships to motion and environmental shear. *Mon. Wea. Rev.*, **142**, 1290–1311, doi:10.1175/MWR-D-13-00249.1.
- Vigh, J. L., and W. H. Schubert, 2009: Rapid development of the tropical cyclone warm core. *J. Atmos. Sci.*, **66**, 3335–3350, doi:10.1175/2009JAS3092.1.
- Wang, Y., and G. J. Holland, 1996: Tropical cyclone motion and evolution in vertical shear. *J. Atmos. Sci.*, **53**, 3313–3332, doi:10.1175/1520-0469(1996)053<3313:TCMAEI>2.0.CO;2.
- Willoughby, H. E., F. D. Marks Jr., and R. J. Feinberg, 1984: Stationary and moving convective bands in hurricanes. *J. Atmos. Sci.*, **41**, 3189–3211, doi:10.1175/1520-0469(1984)041<3189:SAMCBI>2.0.CO;2.
- Yuter, S. E., and R. A. Houze, 1995: Three-dimensional kinematic and microphysical evolution of Florida cumulonimbus. Part II: Frequency distributions of vertical velocity, reflectivity, and differential reflectivity. *Mon. Wea. Rev.*, **123**, 1941–1963, doi:10.1175/1520-0493(1995)123<1941:TDKAME>2.0.CO;2.
- Zehr, R. M., 2003: Environmental vertical wind shear with Hurricane Bertha (1996). *Wea. Forecasting*, **18**, 345–356, doi:10.1175/1520-0434(2003)018<0345:EVWSWH>2.0.CO;2.
- Zhang, D.-L., and H. Chen, 2012: Importance of the upper-level warm core in the rapid intensification of a tropical cyclone. *Geophys. Res. Lett.*, **39**, L02806, doi:10.1029/2011GL050578.
- Zhang, J. A., and E. W. Uhlhorn, 2012: Hurricane sea surface inflow angle and an observation-based parametric model. *Mon. Wea. Rev.*, **140**, 3587–3605, doi:10.1175/MWR-D-11-00339.1.
- , R. F. Rogers, D. S. Nolan, and F. D. Marks Jr., 2011: On the characteristic height scales of the hurricane boundary layer. *Mon. Wea. Rev.*, **139**, 2523–2535, doi:10.1175/MWR-D-10-05017.1.
- , —, P. Reasor, E. Uhlhorn, and F. D. Marks Jr., 2013: Asymmetric hurricane boundary layer structure from dropsonde composites in relation to the environmental wind shear. *Mon. Wea. Rev.*, **141**, 3968–3984, doi:10.1175/MWR-D-12-00335.1.